

JPRS-CST-91-019
18 OCTOBER 1991



JPRS Report

Science & Technology

***China
High-Power Lasers & Laser Fusion Research***

19980203 290

DTIC QUALITY INSPECTED 2

DISTRIBUTION STATEMENT A
Approved for public release;
Distribution Unlimited

REPRODUCED BY
U.S. DEPARTMENT OF COMMERCE
NATIONAL TECHNICAL
INFORMATION SERVICE
SPRINGFIELD, VA 22161

Science & Technology China

High-Power Lasers & Laser Fusion Research

JPRS-CST-91-019

CONTENTS

18 October 1991

LF-11 Laser Apparatus Passes Technical Appraisal [Xie Ping, Liu Jianguo; QIANG JIGUANG YU LIZI SHU, Nov 90]	1
Experimental Research on X-Ray Radiation From Hohlraum Targets Irradiated With Two Beams [Sun Kexi, Xu Heping, et al; QIANG JIGUANG YU LIZI SHU, Nov 90]	3
Energy Measurements for $3/2\omega_0$, $2\omega_0$ Harmonic Waves Emitted by Laser-Irradiated Targets [Xie Ping, Zhao Jiawei, et al; QIANG JIGUANG YU LIZI SHU, Feb 91]	9
High-Efficiency Frequency-Doubling System for LF-11 Laser Apparatus Used for ICF Experiment [Wei Xiaofeng, Zhang Xiaomin; QIANG JIGUANG YU LIZI SHU, Feb 91]	14
Picosecond Soft X-Ray Streak Camera Described [Gu Boxun; QIANG JIGUANG YU LIZI SHU, Feb 91]	22
ICF, X-Ray Laser Experiments With LF-12 (Shen Guang) Apparatus Described [Xiao Guan'gen, RENMIN RIBAO, 3 May 91]	23
Additional Note on LF-12 Apparatus [RENMIN RIBAO, 3 May 91]	24
High-Power Nd:YAG Laser With Variable Pulsewidth [Lin Lihuang, Ouyang Bin, et al; GUANGXUE XUEBAO, May 91]	24
Absolute Measurement of Laser Energy for 'Shen Guang' High-Power Laser Facility [Lin Kangchun, Shen Liqing; GUANGXUE XUEBAO, May 91]	28
Inhomogeneous Distribution of Electron Density, Strong X-Ray Emission by Laser Irradiated Segmented Planar Target [Feng Xianping, Xu Zhizhan, et al; ZHONGGUO JIGUANG, May 91]	31
Automatic Tuning Picosecond Parametric Laser [He Huijuan, Lu Yutian, et al; GUANGXUE XUEBAO, Jun 91]	31
Additional Details on Domestically Developed 10 kW CO ₂ Laser Revealed [Ji Zhong; ZHONGGUO JIGUANG, Jun 91]	35
Broadband Frequency-Doubled Nd:Glass Laser Built at SIOFM [Shang Guang; ZHONGGUO KEXUE BAO, 5 Jul 91]	36
Soft X-Ray Picosecond Framing Camera Developed [Wang Baizhan; ZHONGGUO KEXUE BAO, 19 Jul 91]	36

LF-11 Laser Apparatus Passes Technical Appraisal

91FE0588A Chengdu QIANG JIGUANG YU LIZI SHU
[HIGH-POWER LASER AND PARTICLE BEAMS]
in Chinese Vol 2 No 4, Nov 90 p 513 [inside back cover]

[Article by Xie Ping [6200 1627] and Liu Jianguo [0491 1696 0948]: "LF-11 Laser Apparatus Passes Technical Appraisal"]

[Text] Abstract: The LF-11 laser apparatus (see photos), jointly developed by the Institute of Nuclear Physics and Chemistry of the China Academy of Engineering Physics (CAEP) and by the CAS Shanghai Institute of Optics and Fine Mechanics (SIOFM) passed the technical appraisal held jointly by the two organizations on 12 and 13 July [1990].

The appraisal committee, chaired and vice-chaired by Professor Feng Zhichao [7458 1807 6389] of the University of Electronic Science and Technology, a famous expert in optics, and Research Fellow Jiang Wenhan [1203 2429 3352] of the CAS Chengdu Institute of Optoelectronics, respectively, rigorously reviewed all the major technical specifications of the apparatus. It was unanimously agreed that the apparatus is of excellent quality, with advanced overall technical performance and a high degree of reliability in operation.

The construction of the apparatus began in 1985. Its working medium is silicate neodymium glass and its fundamental frequency optical wavelength is 1.064 μm . The LF-11's initial purpose was to evaluate a variety of diagnostic equipment and testing probes at the Institute of Laser Fusion. After it was completed, with the support of the leadership, the operating staff began to explore and innovate as they carefully operated the apparatus. Based on specific experimental requirements, a series of effective major improvements was made. An automatic focusing and aiming system, an automatic energy-control system, and a 70-mm beam-diameter high-efficiency frequency doubling (0.53 μm) system were developed and perfected for laser-fusion target experiments. With these improvements, not only the quality of the beam but also the stability of the LF-11 have been significantly improved. Presently, the optical energy is steadily tunable between 0 and 50 J at its fundamental frequency. With frequency doubling, its energy is steadily tunable between 0 and 25 J. Its pulsewidth is steadily tunable between 300 and 1200 ps. At its fundamental frequency, the maximum optical power output is $5 \times 10^{10}\text{W}$. With frequency doubling, the maximum optical power output is $3 \times 10^{10}\text{W}$. The beam can be focused to a minimum spot 60 μm in diameter on the target. the laser signal-to-noise ratio (SNR) is generally above 10^6 , and beam-on-target aiming error is less than 10 μm . It is practical and has a high operating efficiency. As far as the fundamental-frequency power output is concerned, this apparatus is only next to the "Shen

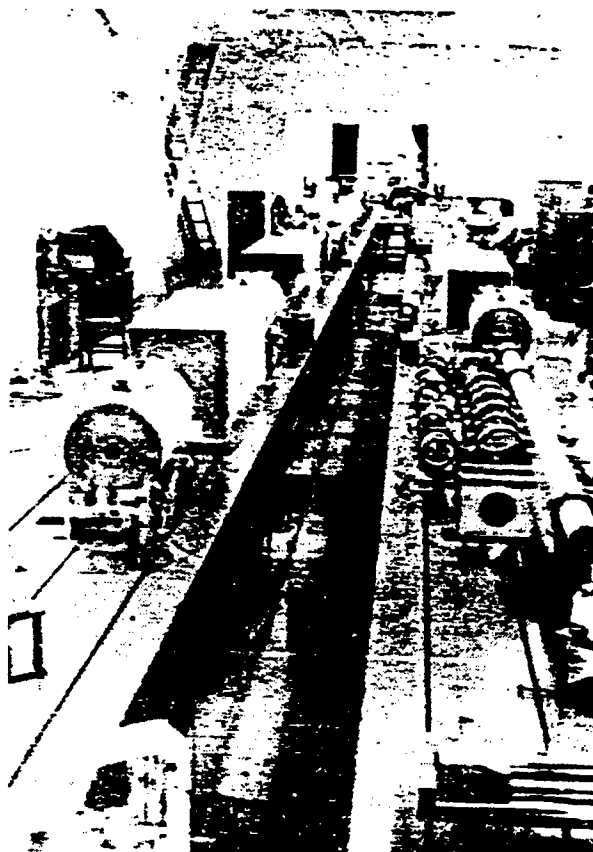


Figure 1. Overall Photograph of LF-11 Laser Apparatus
Guang" ["Magic Light"] apparatus. It is the second-highest-power laser in China.

Since its completion, more than a dozen medium-scale comprehensive physical experiments have been successfully done with this apparatus. It was successfully used to evaluate over a dozen pieces of diagnostic equipment and testing probes. Major experiments conducted include 108.9-nm laser gain with a photo-ionization pump, 10.57-nm Li-like-Al laser gain with a three-body recombination pump, planar-aperture target experiment to simulate black-hole [i.e., "Hohlraum"] entrance, small black-hole target experiment, laser transmission in the atmosphere, atomic parameter research, laser target-shooting characteristics with frequency-doubled neodymium laser, etc. The probes evaluated include a sub-K [sub-keV] X-ray streak camera, a sub-K X-ray spectrometer, optical multichannel analyzer, crystallograph, grating spectrograph, GaAs photoelectric conductivity detector, Faraday charge collector, miniature X-ray diode, heat-release calorimeter, ionograph, etc.

The successful operation and improvement of the apparatus not only play a pivotal role in research on inertial confinement fusion and X-ray lasers but also give us a great deal of experience in the development of high-power laser technology.

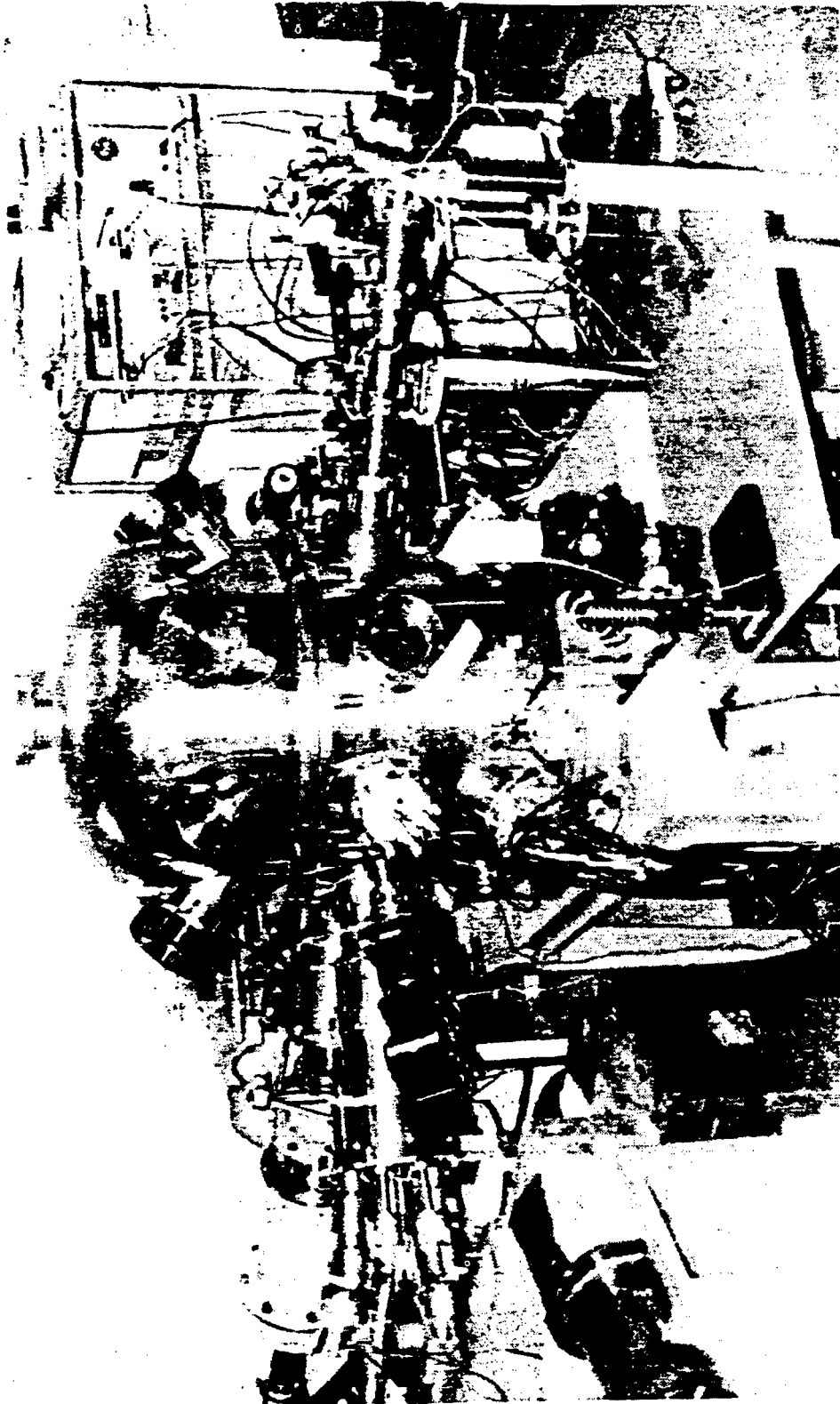


Figure 2. LF-11 Laser Apparatus Target Chamber and Some Diagnostic Equipment

Experimental Research on X-Ray Radiation From Hohlraum Targets Irradiated With Two Beams

91FE0588B Chengdu QIANG JIGUANG YU LIZI SHU [HIGH-POWER LASER AND PARTICLE BEAMS] in Chinese Vol 2 No 4, Nov 90 pp 401-408 [MS received 9 Apr 90, revised 30 Jun 90]

[Article by Sun Kexi [1327 0668 3556], Xu Heping [1776 0735 1627], Tang Yongjiang [0781 3075 0256], Zheng Zhijian [6774 1807 1017], and Yang Jianguo [2799 1696 0948] of the Southwest Institute of Nuclear Physics and Chemistry (SINPC): "Experimental Research on X-Ray Radiation From Hohlraum Targets Irradiated With Two Beams"]

[Text] Abstract: Experimental results of radiation properties of Hohlraum targets irradiated by two laser beams in the Shen Guang apparatus are described. Two sub-keV X-ray spectrometers with time-correlation devices (Dante) were used to monitor the X-ray spectra of the absorption and conversion region and the implosion region. The X-ray pulse waveforms, radiation energy spectra, radiation temperature, radiation time spectra, and radiation temperature versus time were measured. In addition, many hosts with different types of Hohlraum targets were taken to study the relation between radiation temperature in the conversion region and the input laser surface energy density. In this work, for the first time, measurements were made with a grazing incidence grating in the sub-keV X-ray spectrometer and the results obtained were excellent.

I. Introduction

In indirect-drive inertial confinement fusion (ICF) experiments, laser energy is absorbed in the conversion region and then converted into X-rays. In a black-hole cavity, radiation energy is far less than matter energy. The energy is primarily stored in the cavity wall¹:

$$aT_R^4 < \rho c_v T_R \quad (1)$$

where a is the black-body radiation constant, T_R is the radiation temperature, ρ is the density of the cavity wall, and c_v is the specific heat of the matter at constant volume.

Radiation is a means for transferring energy. From the radiational heat transfer equation it is possible to derive an expression for heat transfer at a distance x :

$$x^2 \sim \frac{3l_R c}{b} \frac{4aT_R^3}{\rho c_v} t \quad (2)$$

where l_R is the mean free path of radiation (l_R is proportional to T_R^{-1-3}), c is speed of light, t is the heat

transfer period, and b ranges from 3 to 10. By differentiating equation (2), an expression for the transfer rate x can be obtained:

$$\dot{x} \sim \frac{3l_R c}{b} \frac{4aT_R^3}{\rho c_v x} \quad (3)$$

This equation shows that the transfer rate is proportional to T_R^{4-6} and inversely proportional to the distance. Based on the transfer rate, we know the X-ray flux is

$$F = -k\nabla T_R = -\frac{l_R c}{3} \nabla aT_R^4 \quad (4)$$

This equation shows that the radiation energy transfer flux is proportional to T_R^{5-7} . From these two equations, it is obvious that T_R is a key physical parameter in indirect-drive ICF experiments. In order to attain a good drive field environment to ultimately raise the radiation temperature in the implosion region, we must investigate the laser-to-X-ray conversion mechanism and the radiation transport process. Therefore, it is of significant importance to study the effect of Hohlraum geometry and size on X-ray conversion and radiation transport.^{2,3}

II. Experimental Conditions

1. Layout of Dual-Base Experiment

Figure 1 shows the layout of the dual-beam experiment. Two Dante⁴ spectrometers with time-correlation devices were used to monitor the radiation in two regions. Dante-A has 10 filters and an X-ray diode (XRD) array and is aimed at the laser beam inlet to monitor the X-ray spectrum leaking out of the conversion region. Dante-B has seven filters and an XRD array and is aimed at the diagnostic window in the implosion region to monitor the X-ray spectrum leaking from the implosion region.

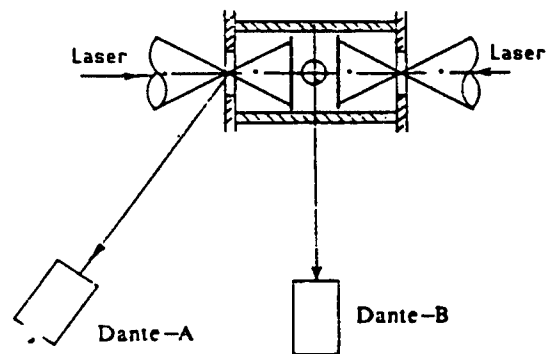


Figure 1. Schematic Diagram of the Dual-Beam Hohlraum Layout

Experiments were done under a variety of conditions with different Hohlraum targets (of different sizes). The experimental layout is essentially to that of the dual-beam black-hole experiment.

2. Spectrometer Improvements

For the first time, a Dante spectrometer is equipped with an X-ray grazing incidence plate mirror.

The plate mirror is based on the principle that when low-energy X-rays travel from a lower-optical density medium to a higher-optical density medium, there is a critical incidence angle above which the X-rays are no longer refracted. Instead, they are totally reflected.

Theoretical calculations show that the critical incidence angle is related to the incident wavelength and atomic number of the plate mirror material. By choosing the suitable material and the proper incidence angle, an ideal X-ray dispersion element can be produced.

Based on machining capabilities in China, we chose nickel as the plate mirror material. It was machined by the [CAS] Changchun Institute of Optics and Fine Mechanics. Its surface roughness is less than 1.5 nm.

The grazing incidence angle of the nickel plate mirror mounted on the Dante spectrometer is 5° . Theoretically, at this angle the mirror has an X-ray cutoff wavelength at 1.65 nm. When the incident wavelength is greater than 1.65 nm, it is totally reflected. Below this wavelength, it is totally cut off. This high-energy cutoff effect of the plate mirror was used to eliminate the high-energy tail in the low-energy detector channel of the spectrometer (see

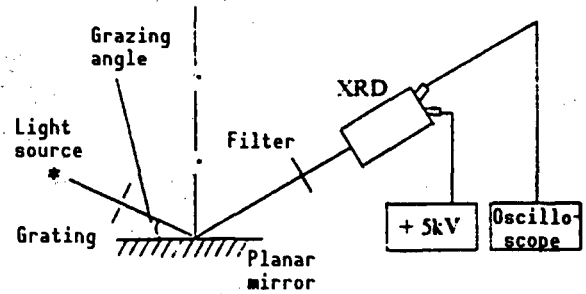


Figure 2. X-Ray Reflection From Grazing Incidence Plate Mirror

Figure 3) which dramatically improved the purity of the low-energy channel and enhanced the accuracy of the energy spectrum. Figure 2 shows a schematic diagram of a low-energy X-ray detection system with a grazing incidence plate mirror. Figure 3 shows response curves of the carbon detector channel with the 5° nickel plate mirror.

3. Time-Correlation Measurement

In order to study the time dependence of X-ray emission and transport properties in Hohlraum experiments, a timing device was installed on the energy spectrum detector system of a sub-keV X-ray spectrometer. A time-resolved recording mode was adopted to show the evolutionary process associated with black-hole radiation.

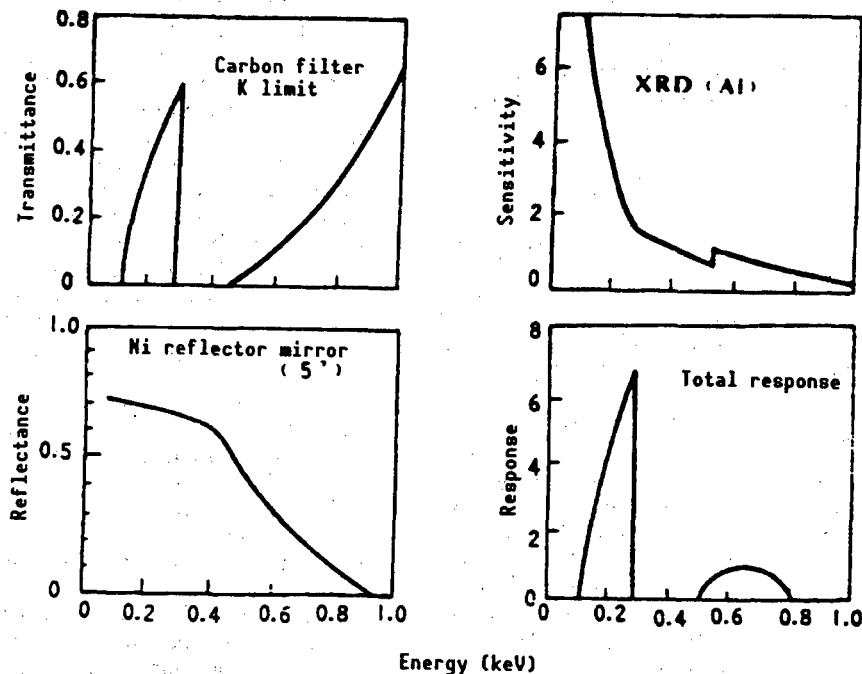


Figure 3. Energy Response Curves in Carbon Detector Channel With 5° Nickel Plate Mirror

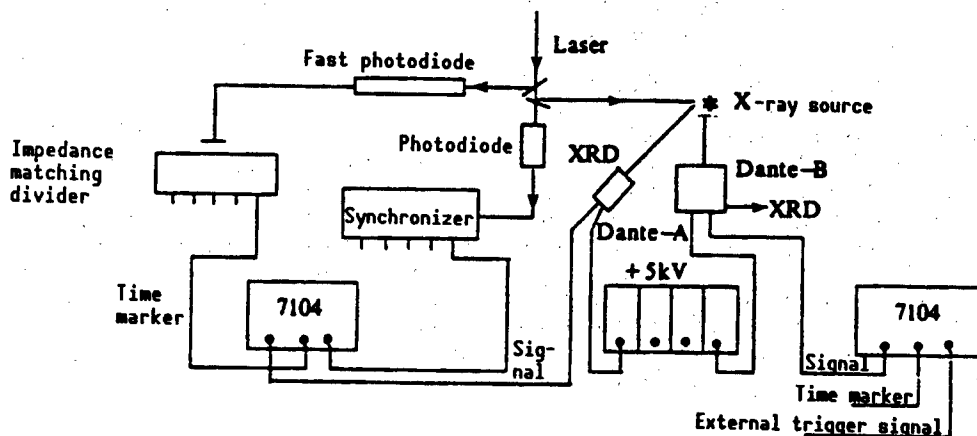


Figure 4. Time Correlation Measurement With Two Spectrometers

In this work, the X-ray pulse from the conversion region received by a detector channel of Dante-A is used as the baseline timing signal. Through an impedance-matching divider, it is applied to the displays of all detector channels in Dante-B. By means of cable delay matching, it is superpositioned onto every record. In order to verify the reliability of this time-correlation method, a laser beam was illuminated on a photodiode. The fast pulse generated by the photodiode was used as the baseline signal. Through a similar impedance-matching divider, it was applied to the display of all detector channels in the two spectrometers and identical results were obtained. Figure 4 shows the schematic diagram of the time correlation measurement with two spectrometers.

4. Experimental Conditions

The black-hole target is shown in Figure 1. The target shell is made of gold and the wall thickness is approximately 10 μm .

The laser wavelength is 1.05 μm , laser energy E_L is approximately 200-500 J/beam, pulsewidth τ_L is about 0.7-1.1 ns, and the lens is $f/1.7$.

The recording devices include (a) eight 500-MHz high-speed (16 lines) oscilloscopes with Polaroid cameras and (b) one (16-channel) fast-pulse charge recorder.

The target number is at $(2-5) \times 10^{-3}\text{Pa}$ vacuum.

III. Experimental Results

Before black-hole target experiments commenced, a gold-plate target was used to set the baseline signal. Under conditions similar to those shown in Figure 1, a shot was taken at a gold-plate target at a 45° incidence angle. Both spectrometers were placed normal to the plate target to simultaneously monitor the X-ray emission from the surface. This time-correlation experiment was used to normalize the timing of the rest of the Hohlraum experiments.

1. Pulse Waveform of X-Rays Emitted in Dual-Beam Hohlraum

The experimental layout is shown in Figure 1. Typical waveforms of X-ray pulses are shown in Figure 5 [photographs omitted]. In all four pictures, the last pulse is the timing pulse which was provided by the carbon detector channel. The signal came from the X-ray leakage from the conversion region. The first pulse is the X-ray from the implosion region which was measured by spectrometer B. Figure 5(a) and (b) are typical X-ray signals from the implosion region with dual laser beams: (a) is the carbon channel (ca. 230-277 eV) signal and (b) is the zinc channel (ca. 650-1012 eV) signal. Figures 5(c) and (d) are typical X-ray signals from the implosion region due to a single laser beam: (c) is the boron channel (ca. 160-183 eV) signal and (d) is the cadmium channel (ca. 400-573 eV) signal. From the dual-beam signals, we can see that the full width at half maximum (FWHM) of the X-ray pulse in the conversion region is greater than that of the X-ray pulse in the implosion region. This is primarily due to the blockage of X-ray transport at the diagnostic window of the implosion region. The plasma cloud generated by expanding hot plasma near the window and by centrifugal motion of the plasma causes the backup. Furthermore, insufficient transport channel and lack of smooth X-ray flow would cause a backup in the cavity which also affects the X-ray emission time in the implosion region.

From the high- and low-energy channel signals of the dual-beam target one can see that the FWHM signal of the low-energy channel is greater than that of the high-energy channel. When radiation temperature gradually falls, the high-energy portion of the radiation energy spectrum decreases even more rapidly, causing the high-energy channel to become narrower.

From the single-beam data one can see that the signal is obviously less than the dual-beam signal at the diagnostic window due to blockage since the cavity and diagnostic window are even smaller. It even oscillates

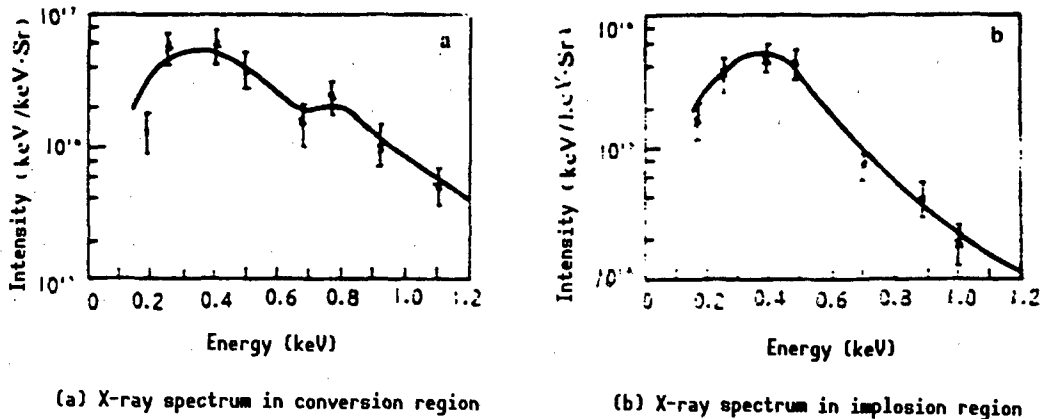


Figure 6. Typical Sub-keV X-Ray Spectra in Dual-Beam Experiment 890531-01

because the plasma cloud first converges toward the window and then diffuses away in an oscillating manner.

2. Sub-keV X-Ray Energy Spectra With Dual-Beam Targets

Figure 6 shows the typical sub-keV X-ray energy spectra obtained in dual-beam experiment 890531-01. Figure 6(a) is the X-ray energy spectrum from the conversion region. It is similar to a gold-plate spectrum with apparent line contribution, especially in the 600-800 eV region in the form of a second peak. This is caused by the N-band emission of gold. Figure 6(b) shows the X-ray spectrum in the implosion region. It is relatively smooth and is close to an equilibrium spectrum.

Figure 6 indicates that the black-hole target plays a confinement role which favors the X-ray relaxation process. The plasma in the cavity gradually reaches equilibrium from nonequilibrium. The radiation also changes from nonequilibrium (mainly X-rays leaking from the conversion region) to equilibrium (mainly X-rays leaking from the implosion region).

3. Time-Resolved Sub-keV X-Ray Spectra

Based on time-resolution measurements, the timing of each channel of Dante-B is normalized. The measured signal underwent Fourier transformation to provide the source function of each channel. Then, the signal within time interval Δt at time t is obtained to determine the X-ray energy spectrum within Δt . We adopted the sand-II scheme developed by W.N. McElory⁵ for this process. In order to overcome instability and "negative energy spectrum" which is not a physical phenomenon and to improve the quality and speed of the iteration process, a technique which involves limited amplitude of iteration and periodic smoothing was employed. Figure 7 shows the typical sub-keV X-ray time spectra and radiation temperature versus time curves in the implosion region of a dual-beam Hohlraum experiment.

From Figure 7(a) we can see that line emission contributes more in the initial stage, especially from the N band

and O band of gold. From the spectrum, the peak is at 300-400 eV, corresponding to the O band. There is a secondary peak at 600-800 eV, corresponding to the N band. During the middle stage of X-ray emission, the contribution of line emission gradually weakens. The spectral intensity increases with higher laser intensity. Within 1.00-1.25 ns, X-ray emission reaches a maximum and the corresponding laser intensity is also the highest. At the late stage, the X-ray spectrum reaches equilibrium again. From Figure 7(b), the radiation temperature versus time curve in the implosion region of a dual-beam target is smoother than that of a plate target. the FWHM of the temperature versus time curve is approximately 2.3 ns. It is only about 2.0 ns for a plate target. Based on this fact, the Hohlraum target has an energy confinement effect. Maintaining a high-temperature radiation field for a longer period of time is the desire of radiation-driven [i.e., indirect-drive] implosion experiments.

4. Effective Radiation Temperature and Its Determination

Based on reference [1], we know that the conversion cavity of a Hohlraum absorbs laser energy. Through electronic heat conduction, the energy is mainly stored in the cavity wall. The energy stored in the cavity wall can be expressed as follows:

$$E_p = x\rho c_V T_R S_{in} \quad (5)$$

where E_p is the energy accumulated in the wall, S_{in} is the inner cavity surface area, and x is the depth of energy storage. By taking the square root of equation (2) we have x is proportional to T_R^{2-3} . Substituting this into equation (5) we get:

$$T_s^{3-4} \text{ is proportional to } E_p/S_{in}$$

With different types (sizes) of Hohlraum experiments, the above theoretical expression was verified. The radiation temperature in the conversion region could be quantitatively determined. Table 1 shows the radiation temperature data of three types of Hohlraum experiments.

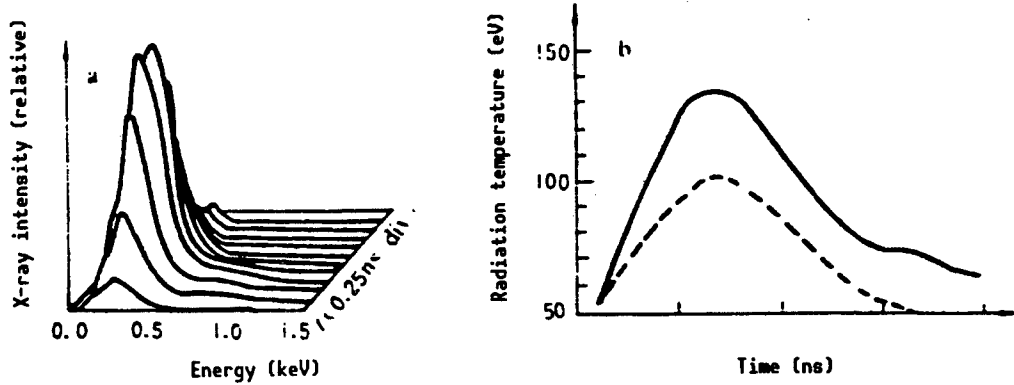


Figure 7. Time-Resolved Spectra of Typical Dual-Beam Experiment 890531-01

Table 1. Experimental Data of Three Types of Hohlraum Experiments

Target	Laser energy (J)	Pulse width (ns)	Conversion region T_{R1} (eV)	Implosion region T_{R2} (eV)
Dual-beam target (large cavity)	427	1.12	148	137
	415	0.98		
Leaky target (medium cavity)	442	0.84	170	—
Single-beam target (small cavity)	434	0.78	176	110

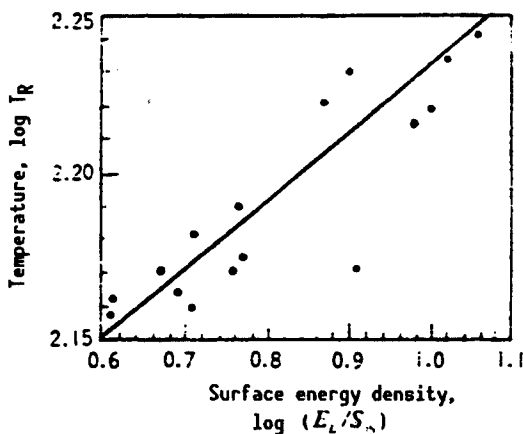


Figure 8. Logarithmic Plot of Conversion-Zone Radiation Temperature Vs. Incident Laser Surface Energy Density. E_L/S_{in} expressed in units of $10^4 J/cm^2$ and T_R in eV.

From Table 1, under almost identical conditions, the different targets have different conversion-region radiation temperature, dependent upon the surface area of the cavity. A large cavity has a larger inner surface area and lower temperature. Conversely, a small inner cavity surface area has a higher temperature. Based on the data, the relation between conversion region temperature and average laser energy density per unit surface area is obtained. Figure 8 shows a logarithmic relation between radiation temperature and mean surface laser energy density.

Based on the curve in Figure 8, through linear regression, the following equation can be derived:

$$T_{R1} = 106 \left(\frac{E_L}{S_{in}} \right)^{0.21} \quad (6)$$

where T_{R1} is the conversion-region radiation temperature, in eV. E_L/S_{in} is in units of $10^4 J/cm^2$, which is the quantity determined by Hohlraum experiments. It is analogous to the theoretical result derived from equation (5).

From Table 1, one also finds that single-beam targets have higher radiation temperature in the conversion region compared to dual-beam targets. However, the radiation temperature in the implosion region is much lower than that of a dual-beam target. This is dependent upon the X-ray transport situation. Because the cavity is small, its transport channel is also limited. The amount of energy delivered into the implosion region is low; thus, the temperature of the radiation field formed is also low. Conversely, a dual-beam target has a larger transport channel which delivers more energy to the implosion region. Therefore, its radiation temperature is also higher.

5. Investigation of Radiation Transport Time

Another objective of the time-correlation experiment is to observe the X-ray transport time. On the basis of the time-correlated X-ray signals emitted from the two

regions of a black-hole target shown in Figure 5, using a plate target signal for time normalization, the time delay between the X-ray pulses emitted from the implosion region and that from the conversion region was measured. This time is the X-ray transport time. The results not only did not reveal any transport time but also showed that the X-rays from the implosion region are ahead of those from the conversion region by 0.1-0.5 ns. Furthermore, this amount increases as the diagnostic window gets smaller. Moreover, this amount is larger for lower-energy channels. An analysis showed that this is a false impression due to a bottleneck. The trailing edge of the real pulse is absorbed by the ion cloud which creates the false impression that the peak of the pulse is shifted forward. The bottleneck effect occurs even earlier when the diagnostic window is small. (The ion cloud gathers at the center of the diagnostic window faster.) Even the real pulse peak is absorbed, as shown in Figure 5(c) and (d) with a single-beam target. At this time, when the ion cloud emits, X-rays can pass through the window again. This creates the oscillation patterns shown in Figure 5(c) and (d).

This result qualitatively indicates that the X-ray transport time is relatively small. Otherwise, the forward shift (impression) of the X-ray pulse created by the diagnostic window of the implosion region would not be so apparent. It is estimated to be less than 0.1 ns.

IV. Conclusions

Dual-beam Hohlraum experiments revealed that laser absorption and X-ray conversion might be more efficient when the conversion cavity is large and the mean surface density of injected laser energy is low. However, it is difficult to establish a high-temperature field which hinders the transport speed and X-ray flux. Nevertheless, from the radiation temperatures for different cavities shown in Table 1, dual-beam targets have larger conversion cavities and transport windows. The transport channels are wide open and the energy delivered to the implosion region is also high. The radiation temperature established is higher than that of a small-cavity single-beam target. Different outcomes were obtained with similar targets of various transport windows. This result also explains the same effect from another viewpoint.

In conclusion, conditions that affect conversion, radiation transport, and radiation temperature are mutually constraining. It is impossible to pursue one condition while neglecting others. All factors must be considered in the design in order to obtain the optimum radiation-drive environment.

Sub-keV X-ray energy and time spectra of dual-beam Hohlraum experiments show that there was a great deal of line radiation in the X-ray conversion process, especially in the initial stage. In the 300-400 eV and 600-800 eV ranges, the contribution of line radiation is more prominent. It corresponds to the O band and N band emission of gold. This indicates that the gold plasma was

not fully ionized under the experimental condition (approximately 130-170 eV in plasma radiation temperature). Most transition lines occurred in fourth or fifth shells.

The time spectra also revealed the X-ray relaxation process. In the initial stage (within 1.0 ns), although X-ray intensity rises with increasing laser intensity, line emission gradually weakens from a dominant position. After 1.0 ns, X-ray emission reaches equilibrium. This is the X-ray relaxation process and the relaxation time is approximately 1.0-1.5 ns.

Use of a 5° nickel-plate mirror could improve the purity of a low-energy channel from 50 percent to above 90 percent. Only a very small portion of the high-energy tail is still contributing to the signal. In order to further improve the purity of the low-energy channel signal, it is necessary to develop plate mirrors made of lighter materials (such as carbon, beryllium, etc.) to completely eliminate the high energy tail.

Acknowledgement

The authors wish to express their gratitude to the target fabrication group, Laboratory 209, SINPC, for providing a large number of different targets; to Laboratory 210 and to Shanghai Joint Laser Laboratory for operating the laser; to the leadership of the institutes involved for their support; and to Chang Fuhua [1603 1381 5478] of Laboratory 204 for making a large number of filters.

References

1. Yu Min [0060 2404], "Outlook for Inertial Confinement Fusion," China Academy of Engineering Physics, CAEP-0001, HL-0001, Jan 1988.
2. Zhang Yun [1776 6874], et al., "Study of Laser X-Ray Conversion in Cylindrical Cavity Targets and Related Physical Problems," Symposium of Annual High-Power Laser Technology Conference (2), Apr 1988.
3. Chang Tieqiang [1603 6993 1730], et al., "Physical Processes in High-Gain, Indirect-Drive Inertial Confinement Fusion," QIANG JIGUANG YU LIZI SHU [HIGH-POWER LASER AND PARTICLE BEAMS], Vol 1 No 3, 1989.
4. Sun Xexi, et al., "Diagnosis of Laser Plasma Using Sub-keV X-Ray Energy Spectrum," Ibid., Vol 2 No 1, 1990.
5. W.N. McElroy, et al., "A Computer-Automated Iterative Method for Neutron Flux Spectral Determination by Foil Activation II, Sand II," New Mexico, 1967.

Energy Measurements for $3/2\omega_0$, $2\omega_0$ Harmonic Waves Emitted by Laser-Irradiated Targets

91FE0588C Chengdu QIANG JIGUANG YU LIZI SHU [HIGH-POWER LASER AND PARTICLE BEAMS] in Chinese Vol 3 No 1, Feb 91 pp 50-56 [MS received 11 Apr 90, revised 10 Sep 90]

[Article by Xie Ping [6200 1627], Zhao Jiawei [6392 0857 0251], Yang Xiangdong [2799 0686 2639], Zhang Haiying [1728 3189 5391], and Guo Su [6753 4790] of SINPC: "Energy Measurements for $3/2\omega_0$ and $2\omega_0$ Harmonic Waves Emitted by Laser-Irradiated Targets"]

[Text] Abstract: The principle and method of energy measurement for the $3/2\omega_0$ and $2\omega_0$ harmonic waves emitted by planar and Hohlraum targets irradiated with the fundamental-frequency ($\lambda = 1.053\ \mu\text{m}$) "Shen Guang" Nd-glass laser are described. Experimental results are presented. In addition, a brief analysis and discussion are also provided.

I. Introduction

In laser-fusion experiments, superthermal electrons are an important issue. A large number of experiments conducted in recent years show that the temperature and number of superthermal electrons generated by irradiating Hohlraum targets are much higher than the temperature and number of superthermal electrons generated by planar targets under identical conditions. This effect has seriously threatened our future work on laser-induced fusion. In order to suppress superthermal electrons and minimize the deleterious effect, it is imperative for us to understand its generation mechanism. Based on theory,¹ under conditions relevant to the Shen Guang apparatus, superthermal electrons might be generated in a Hohlraum target from excited Raman scattering or resonant absorption. However, it is difficult to determine which one is the dominant mechanism, or whether there are other important mechanisms, based on theory alone. We have to depend upon experimental data to reach a decision. To this end, we installed probes specifically designed to measure $3/2\omega_0$ and $2\omega_0$ (ω_0 is the fundamental frequency) harmonic waves in order to observe the energy associated with products of the duoplasma decay process at $3/2\omega_0$ and the energy associated with products of the resonant absorption process at $2\omega_0$.

There are only a few reports published in other countries on the measurement of characteristics of $3/2\omega_0$ and $2\omega_0$ harmonic waves emitted by a planar target irradiated at the fundamental frequency.^{2,3,4} The measurement of characteristics of $3/2\omega_0$ and $2\omega_0$ harmonic waves emitted by a Hohlraum target irradiated at the fundamental frequency has not been reported at all. Prior to this experiment, we had no idea about the amounts of energy associated with the $3/2\omega_0$ and $2\omega_0$ harmonic waves for planar and Hohlraum target irradiated by the "Shen Guang." In order to ensure a high SNR, to set a reasonable measurement range for the data recording system and to prepare the proper filters for the probes, we examined a great deal of target data⁴ obtained with

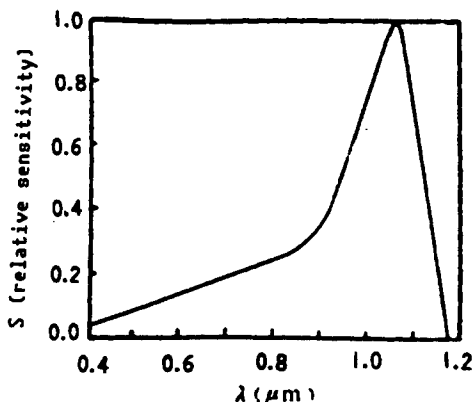


Figure 1. Spectral Response Curve of Silicon Photodiode

high-power lasers. We assumed that the energy of either the $3/2\omega_0$ or $2\omega_0$ harmonic waves is lower than that of Raman, at below 10^{-6} .

Under the circumstance that the excited Brillouin scattering background is seriously present, it is relatively difficult to accurately determine the amounts of energy associated with $3/2\omega_0$ and $2\omega_0$. Nevertheless, we managed to maintain a sufficient SNR by using bandpass filters and neutral density filters and by adjusting the sensitivity of the recording system we obtained very good data.

II. Probe Structure and Sensitivity Determination

With fundamental frequency irradiation, the characteristic wavelengths of the $3/2\omega_0$ and $2\omega_0$ harmonic waves are $0.71\ \mu\text{m}$ and $0.53\ \mu\text{m}$, respectively. Both wavelengths are within the sensitivity range of the silicon photodiode. Therefore, silicon photodiodes with filters are used to measure the energy of $3/2\omega_0$ and $2\omega_0$ harmonic waves at various points in space. Furthermore, the total energy emitted by harmonic waves in space is estimated based on the angular distribution curve thus measured.

Probes are made of PIN silicon photodiodes together with bandpass filters and multiple layers of neutral density filters. Figure 1 shows the spectral response curve of the silicon photodiode (provided by the manufacturer Chengdu Radio Plant No. 3). Figures 2 and 3 show the typical transmittance curves with band filters for $3/2\omega_0$ and $2\omega_0$, respectively.

In order to ensure sufficient SNR, comprehensive consideration has been given to the composite filters for the probes. The SNR of the $3/2\omega_0$ and $2\omega_0$ harmonic wave probes is better than 50 with respect to scattered $1\omega_0$ light. The $3/2\omega_0$ probe has an SNR of over 100 with respect to $2\omega_0$ harmonic waves and Raman scattering. The $2\omega_0$ probe also has an SNR of over 100 with respect to $3/2\omega_0$ harmonic waves and Raman scattering.

The FWHM ($\Delta\lambda$) of the bandpass filter is chosen based on the planar target data given in Reference [4]. The

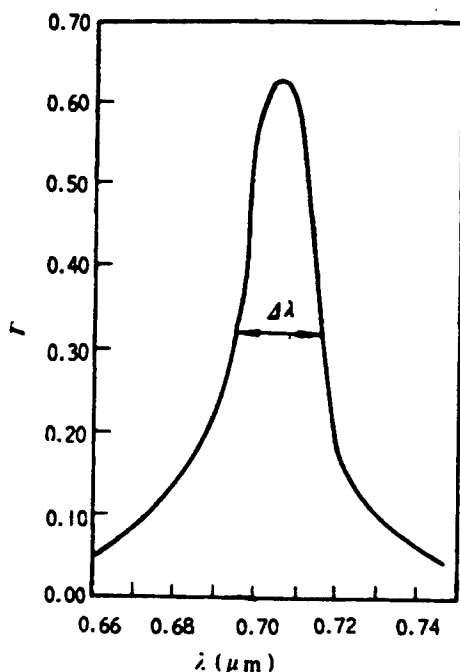


Figure 2. Transmittance Curve for Bandpass Filter on $3/2\omega_0$ Probe

passband FWHM of the filter is slightly larger than the overall width of the harmonic wave to be measured.

Before the experiment, a 50-mm diameter frequency-doubled beam from the LF-11 laser was used to calibrate the sensitivity of the $2\omega_0$ probe. A 70-mm diameter fundamental frequency beam and a frequency-doubled beam from LF-11 were used to calibrate the sensitivities of the silicon photodiode of the $3/2\omega_0$ harmonic wave probe at $1\omega_0$ and $2\omega_0$. Based on the calibration data,

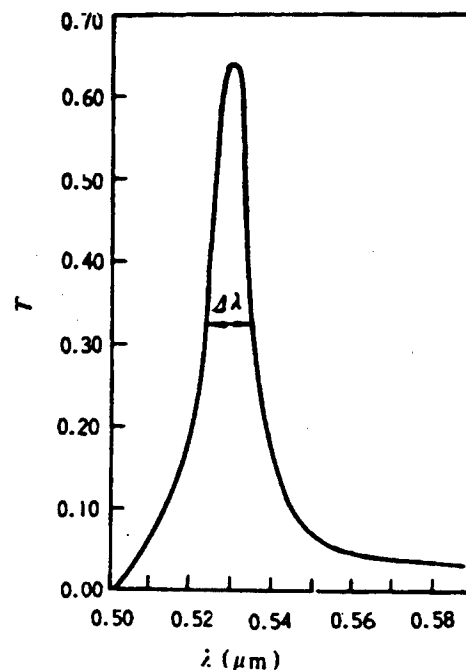


Figure 3. Transmittance of Bandpass Filter on $2\omega_0$

together with the curve shown in Figure 1 and the transmittance of the filter, the sensitivity of the $3/2\omega_0$ probe can be determined.

III. Experimental Conditions and Method

The experiment was carried out on the "Shen Guang" apparatus. For ease of comparison, gold Hohlraum targets, gold planar targets, and aluminum planar targets were irradiated under essentially identical conditions as shown in Table 1. In Table 1, E_L , τ_L , σ , SNR, P, and D/f are incident laser energy, laser pulsewidth, laser focal spot, laser signal-to-noise ratio, target vacuum, and relative aperture of target lens, respectively.

Table 1. Irradiation Parameters of "Shen Guang" Apparatus

E_L (J)	τ_L (ps)	σ (μm)	SN	p (Pa)	D/f
142-442	620-940	ca. 200	10^7	1.33×10^{-3}	f/1.7

In order to measure the angular energy distribution of the two harmonic waves, the two types of probes are laid out in the manner shown in Figure 4.

Since the target chamber has very limited room, in order to accommodate other tests, we placed seven $3/2\omega_0$ probes and six $2\omega_0$ probes. Five of the seven $3/2\omega_0$ probes were installed on the same rack to measure the energy distribution of $3/2\omega_0$ as a function of angle θ . The remaining two were placed on an opposite probe rack to measure the symmetry of energy distribution of $3/2\omega_0$ with respect to ϕ . Five of the six $2\omega_0$ probes were installed on the same rack to measure the energy distribution of $2\omega_0$ harmonic wave as a function of angle θ .

The last one was placed on an opposite probe rack to measure the symmetry of energy distribution of $2\omega_0$ with respect to ϕ . All probes were slanted to minimize the energy integration error due to the difference in energy distribution on polarized and nonpolarized planes. (In this paper, θ is the angle between the line connecting the point of observation to the center of the target and the normal of the target, or the center line of the incident aperture. ϕ is defined as the angle between the projection of the line connecting the point of observation to the target center on the XY plane and the X-axis in a three-dimensional coordinate system where the Z-axis is normal to the target or is the center line of the incident aperture and Y-axis is pointing toward the top of the target chamber.)

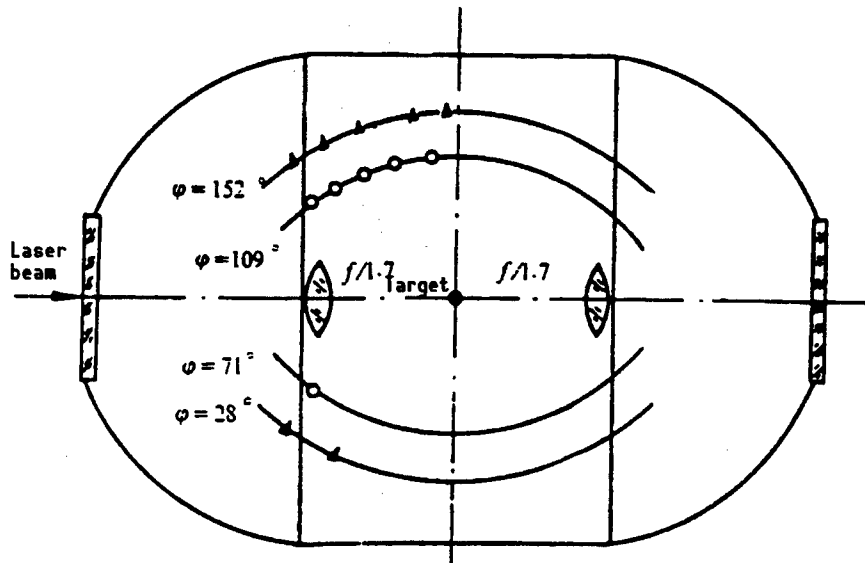


Figure 4. Layout of Harmonic Wave Probes ("Δ" is $3/2\omega_0$ probe and "O" is $2\omega_0$ probe)

IV. Experimental Results

1. Angular Distribution of Energy

It was found that under similar irradiation conditions and out-of-focus degree, the θ distribution of either harmonic wave from a Hohlraum target is more gradual than that from a planar target. The intensity increases monotonically with $\cos\theta$ for a Hohlraum target. The $3/2\omega_0$ harmonic wave of a planar target also increases with $\cos\theta$. However, the intensity of the $2\omega_0$ harmonic wave peaks near $\theta = 45^\circ$. Typical results are shown in Figures 5, 6, and 7.

It was also experimentally observed that the intensity of both harmonic waves also increases monotonically with $\cos\theta$. Typical results are shown in Figure 8.

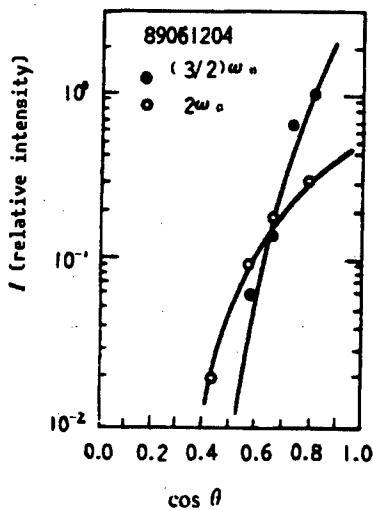


Figure 5. Typical Harmonic-Wave Energy Distribution of Hohlraum Target vs. θ

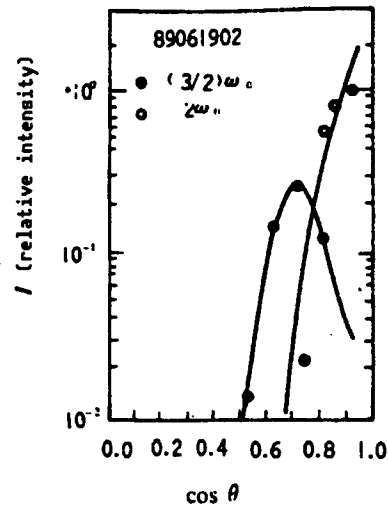


Figure 6. Typical Harmonic-Wave Energy Distribution of Out-of-Focus Planar Gold Target Vs. θ

It was experimentally observed that the intensity distribution of either harmonic wave is essentially symmetric with respect to ϕ regardless of planar or Hohlraum targets.

2. Total Energy

It was found that the total energy emitted by the two harmonic waves is very low by either a planar or Hohlraum target. Under conditions given in Table 1, the total energy of the $2\omega_0$ harmonic wave is 0.1-0.5 J and that of the $3/2\omega_0$ harmonic wave is 0.2-2 J. Table 2 shows some typical energy data.

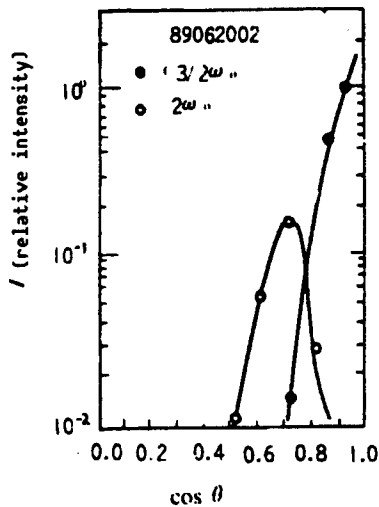


Figure 7. Typical Harmonic-Wave Energy Distribution of Out-of-Focus Planar Aluminum Target Vs.

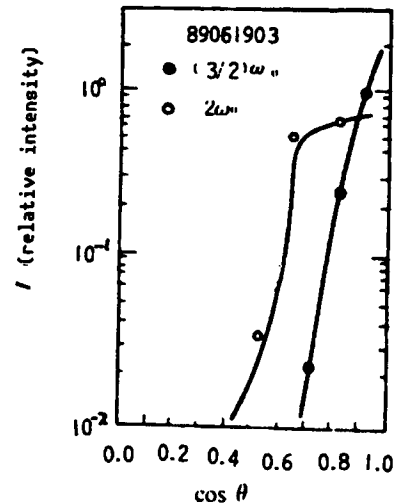


Figure 8. Typical Harmonic-Wave Energy Distribution of Focal-Spot Planar Gold Target Vs.

Table 2. Typical Harmonic-Wave Energy Values for Different Targets

Target type	Experiment No.	E_L (J)	τ_L (ps)	I_L (W/cm ²)	$E_{3/2\omega_0}$ (J)	$E_{2\omega_0}$ (J)
Hohlraum	89061203	332.8	810	1.15×10^{15}	1.381	0.341
Gold planar	89061901	361.1	620	1.59×10^{15}	0.336	0.109
Aluminum planar	89062002	338.7	870	1.06×10^{15}	0.664	0.269

3. Energy Ratio and Its Dependence on Incident Laser Power Density

It was found that the energy ratio of the $3/2\omega_0$ harmonic wave (as a fraction of incident laser energy) is approximately three to five times higher than that of the $2\omega_0$ harmonic wave when a Hohlraum target is irradiated out of focus. It is approximately two to four times higher than that of the $3/2\omega_0$ harmonic wave of a gold planar target and is two to three times higher than that of an aluminum planar target. The energy ratio of the $3/2\omega_0$

harmonic wave of either gold or aluminum planar target is higher or slightly higher than that of the energy ratio of its $2\omega_0$ harmonic wave. When the target is irradiated in focus, the energy ratio of the $3/2\omega_0$ harmonic wave is essentially the same as that of the $2\omega_0$ harmonic wave for gold planar targets, as shown in Table 3. In the table, I_L represents the mean laser power density of several shots fired under similar conditions ($E_L = 300$ - 400 J, $\tau_L = 700$ - 800 ps). $\epsilon_{3/2\omega_0}$ and $\epsilon_{2\omega_0}$ are the mean energy ratios of $3/2\omega_0$ and $2\omega_0$ harmonic waves, respectively.

Table 3. Energy Ratios of Harmonic Waves of Different Targets

Target type	Laser focus state	I_L (W/cm ²)	$\epsilon_{3/2\omega_0}$	$\epsilon_{2\omega_0}$
Hohlraum	300 μ m out of focus	1.15×10^{15}	3.88×10^{-3}	1.06×10^{-3}
Gold planar	300 μ m out of focus	1.47×10^{15}	7.95×10^{-4}	3.13×10^{-4}
Al planar	300 μ m out of focus	1.13×10^{15}	1.42×10^{-3}	5.38×10^{-4}
Gold planar	Focused	3.46×10^{16}	1.26×10^{-3}	8.33×10^{-4}

It was also observed that the energy ratios of either planar or Hohlraum targets climbed with increasing incident laser power density. However, the increase is not linear. Figures 9 and 10 are typical plots for energy

ratio versus incident laser power density for the two harmonic waves emitted by Hohlraum targets. The curves are drawn based on functions derived from least squares fit of the data points.

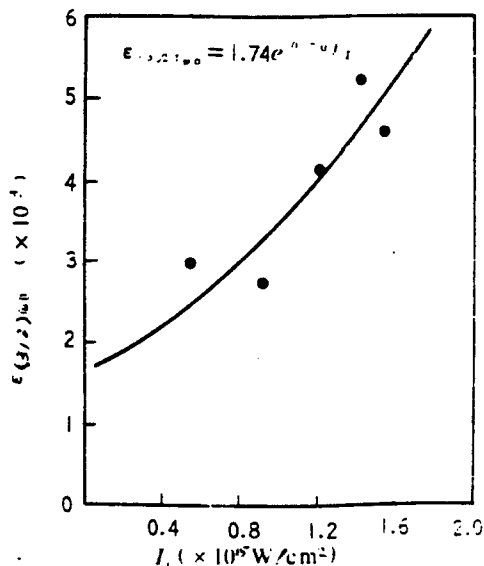


Figure 9. $3/2\omega_0$ Harmonic-Wave Energy Ratio Vs. Laser Power Density on First Irradiation Surface of Hohlraum Targets

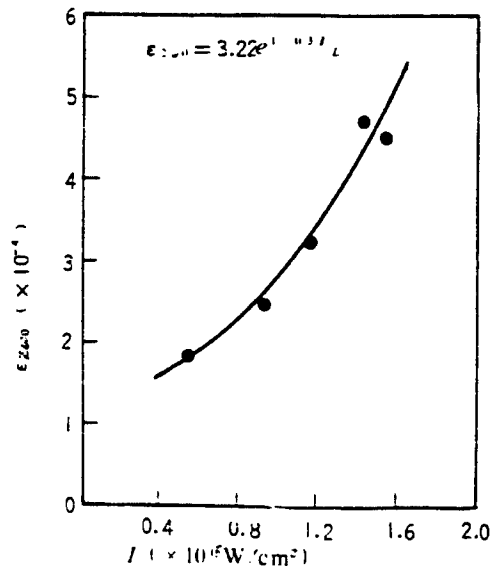


Figure 10. $2\omega_0$ Harmonic-Wave Energy Ratio Vs. Laser Power Density on First Irradiation Surface of Hohlraum Targets

V. Analysis and Discussion

Several physical processes take place after the laser interacts with the target material, including stimulated Brillouin scattering, stimulated Raman scattering, duoplasma decay, ion-acoustic decay, filament formation, and resonant absorption. Ion-acoustic decay and resonant absorption take place near the critical surface and can produce $1\omega_0$ electron plasma waves. Stimulated Raman scattering and duoplasma decay take place at below one-quarter critical surface and near one-quarter critical surface, respectively. Both processes will produce $1/2\omega_0$ electron plasma waves. Coupling of the incident light with $1\omega_0$ electron plasma waves produces $2\omega_0$ harmonic waves and coupling of the incident light with $1/2\omega_0$ electron plasma waves produces $3/2\omega_0$ harmonic waves. The energy ratio [i.e., portion] of the $3/2\omega_0$ harmonic wave emitted by out-of-focus planar and Hohlraum targets is substantially higher than that of the $2\omega_0$ harmonic wave. This indicates that for these two types of targets irradiated by a large light spot, stimulated Raman scattering and duoplasma decay are significantly more predominant than processes such as resonant absorption, ion-acoustic decay, and filament formation. They become the primary processes to produce superthermal electrons. When a planar target is irradiated with a focused beam, the energy ratio of the $2\omega_0$ harmonic wave is essentially identical to that of $3/2\omega_0$ harmonic wave. This effect indicates that in a planar target irradiated by a small focused-spot beam, nonlinear processes near the critical surface such as resonant absorption have become competing mechanisms against stimulated Raman scattering and duoplasma decay to generate superthermal electrons. Mei Qiyong [2734 0796 1661], et al., measured the total amounts of energy associated with stimulated Raman scattering for various types of targets and

the spectra of stimulated Raman scattering and $3/2\omega_0$ and $2\omega_0$ harmonic waves.⁵ Their energy measurement result shows that the energy ratio of Raman scattering is over 5 percent for Hohlraum targets and 3×10^{-3} for planar targets with out-of-focus irradiation. When irradiated with focused light, the Raman energy ratio of a gold planar target is approximately 6×10^{-4} . A comparison of this result with the harmonic wave energy data measured in this work shows that stimulated Raman scattering is the primary mechanism to produce superthermal electrons in planar and Hohlraum targets irradiated with a large light spot. In planar targets irradiated with focused light, resonant absorption is one of the important superthermal electron-producing mechanisms only next to duoplasma absorption.

Under identical experimental conditions, the energy ratios of $3/2\omega_0$ and $2\omega_0$ harmonic waves emitted by a Hohlraum target are substantially higher than those emitted by a planar target of the same material. This fully demonstrates that processes such as stimulated Raman scattering, duoplasma decay, resonant absorption, ion-acoustic decay, and filament formation in Hohlraum targets are significantly better than those in planar targets. This is the reason the temperature and number of superthermal electrons in a Hohlraum target are substantially higher than those in a planar target. These nonlinear processes are more intense in harmonic waves because of multiple interactions of the laser in the cavity which lowers the plasma density gradient in the target and procures a larger space for those nonlinear processes to take place.

The energy ratios associated with Raman scattering and $3/2\omega_0$ harmonic waves are significantly higher than the energy ratio of $2\omega_0$ harmonic waves for Hohlraum

targets. This indicates that Hohlraum targets have a relatively abundant amount of dilute plasma. It also indicates that the critical density region in a Hohlraum target is much narrower than the quarter critical density region and that of the region below one-quarter critical density.

The energy ratios of the two harmonic waves for gold planar targets are substantially lower than those of aluminum planar targets because gold has a higher plasma-collision frequency due to its high atomic number (ν^{ei} is proportional to z). This higher plasma-collision frequency suppresses the progress of various collective interactions.

With similar energy and pulsewidth, the energy ratios of harmonic waves for a planar target irradiated by a focused beam are significantly higher than those for a planar target irradiated by an out-of-focus beam. This indicates that various nonlinear processes are closely dependent upon the laser power density on the target surface.

The effect that the energy ratio of harmonic wave emitted by a Hohlraum target increases nonlinearly with the laser power density on the first incident surface is caused by the fact that electron plasma waves at different frequencies increase nonlinearly with rising laser power density.

The $2\omega_0$ harmonic wave of a planar target irradiated by an out-of-focus beam is most intense at $\theta = 45^\circ$. This indicates that nonlinear processes such as resonant absorption are especially active at $\theta = 45^\circ$. The $2\omega_0$ harmonic wave for a Hohlraum target is most intense at $\theta = 0^\circ$. This is because most $2\omega_0$ photons tend to move toward the center of the aperture as they escape.

Before this work began, it was observed with the naked eye that the green light emitted by Hohlraum targets was much stronger than that from planar targets. This observation was confirmed by experimental data. The data also showed that the $3/2\omega_0$ harmonic wave for a Hohlraum target is substantially stronger than the $2\omega_0$ harmonic wave. This effect was not noticed by the naked eye because the response to the $3/2\omega_0$ light is much lower than the response to the $2\omega_0$ by the human eye.

The angular distribution data for both harmonic waves measured in this work is found to be in good agreement with the corresponding spectral intensity distribution data obtained by Mei Qiyong.

The experimental error in this work includes probe calibration error, probe photodiode spectral-response curve error, probe-positioning error, filter transmittance error, recording system error, and data processing error. These errors are estimated to be ± 10 , ± 5 , ± 3 , ± 5 , ± 4 , and ± 7 percent, respectively. Therefore, the relative errors for the measurement of total energy of $3/2\omega_0$ and $2\omega_0$ harmonic waves are ± 15 and ± 14 percent, respectively.

The authors wish to thank Zheng Zhijian [6774 1807 1017] and Jin Genzhi [6855 2704 5347] for their assistance as well as the people involved in the operation and target fabrication for the LF-11 and "Shen Guang" facilities.

References

1. Liu Chenghai [0491 2052 3189], et al., "Superthermal Electrons in Black-Hole Targets," internal report of Beijing Institute of Applied Physics and Computational Mathematics, Apr 1987.
2. S.S. Glaros, V.C. Rupert, and S.R. Gunn, "Energy Balance Measurements for Shiva," Physics and Astronomy Classification Scheme Number 52.
3. D.M. Woodall and B. Yaakobi, "Emission of Laser Harmonics," Laser- Induced Fusion and X-Ray Laser Studies, pp 191-218.
4. R.L. Turner, " $3/2\omega_0$ Emission at $1\omega_0$ and $2\omega_0$," Laser Program Annual Report, 1981, pp 6-27.
5. Mei Qiyong, et al., "Experimental Study of Stimulated Raman Scattering," internal report, SINPC, Jan 1990.

High-Efficiency Frequency-Doubling System for LF-11 Laser Apparatus Used for ICF Experiment

91FE0588D Chengdu QIANG JIGUANG YU LIZI SHU [HIGH-POWER LASER AND PARTICLE BEAMS] in Chinese Vol 3 No 1, Feb 91 pp 85-94 [MS received 9 Apr 90, revised 27 Jun 90]

[Article by Wei Xiaofeng [7614 2556 1496], Zhang Xiaomin [1728 1420 3046], Yuan Xiaodong [5913 2556 2639], Ye Jinxiang [0673 6855 4382], and Sui Zhan [7131 1455] of China Academy of Engineering Physics (CAEP): "High-Efficiency Frequency-Doubling System for LF-11 Laser Apparatus"]

[Text] Abstract: The design principle and structure of a high-efficiency frequency-doubling system for the LF-11 laser apparatus, as well as various technical approaches to achieving high-efficiency frequency-doubling, are described. The frequency-doubling conversion efficiency, the tuning half width of the crystal, the far-field divergence angle of the fundamental-frequency laser and frequency-doubled laser, the near-field intensity distribution, and the time profile were measured. The system was used to perform 0.53- μm wavelength inertial-confinement fusion (ICF) experiments.

I. Introduction

Experimental laser plasma physics studies continue to demonstrate the superiority of using a short-wavelength, high-power laser to irradiate targets because it can significantly reduce the number of deleterious high-energy electrons produced. This allows us to concentrate on fluid dynamics and radiation propagation and not worry about the effect of thermal electrons. Moreover, it can substantially raise the absorption of the laser beam,

improve X-ray conversion efficiency, and effectively reduce back-scattering of the laser.

Presently, many laboratories in other countries are using large-aperture nonlinear crystals to achieve high-efficiency frequency-doubling and frequency-tripling^{1,2,3} for high-power Nd-glass laser apparatus. Several studies⁴⁻⁷ on the frequency-doubling of high-power lasers have been done in China as well. However, these studies were done with small apertures and low intensity and could not be used in experimental apparatus for ICF studies. In order to meet the high-tech requirements for ICF experiments, on the basis of frequency-doubling experiments carried out with a 50-mm diameter KDP [potassium dihydrogen phosphate] crystal and the characteristics of the LF-11 laser apparatus, we developed China's first high-efficiency frequency-doubled system for a high-power Nd-glass laser using 70-mm diameter KDP crystal. The system was used to perform ICF experiments at 0.53 μm . This has laid a solid foundation for a frequency-tripled system.

II. Description of the Frequency-Doubling System

The nominal power output for LF-11 is 10^{11}W and its wavelength is 1.064 μm . The last-stage output aperture is 64 mm, the far-field divergence angle is 0.15-0.4 mrad,

and the pulsewidth is 200-800 ps. Based on these basic parameters, a frequency-doubling system is mainly comprised of a frequency doubler, collimating system, laser parametric measurement system, and automatic thermostat system. The overall layout is shown in Figure 1.

1. Frequency Doubler

Type-II matching KDP crystals, 70 mm in diameter and 14 mm and 16 mm in thickness are used for frequency-doubling. In order to avoid deliquescence of the crystal and to minimize Fresnel reflection loss at its end, the crystal is sealed in a container filled with a liquid of matching index of refraction. The input and output ends of the crystal box are coated with double antireflective coatings at 1.06 μm and 0.53 μm , respectively (see Figure 2). In order to ensure safe operation of the KDP crystal at high power, the entire assembly is done in an ultraclean environment. The overall transmittance of the frequency doubler is $\tau_{1.06} = 98\%$ at 1.064 μm and $\tau_{0.53} = 96\%$ at 0.532 μm .

2. Collimating System

The type II matching mode is critical phase matching. In order to accurately adjust the phase-matching angle of the crystal, the frequency doubler is mounted on a

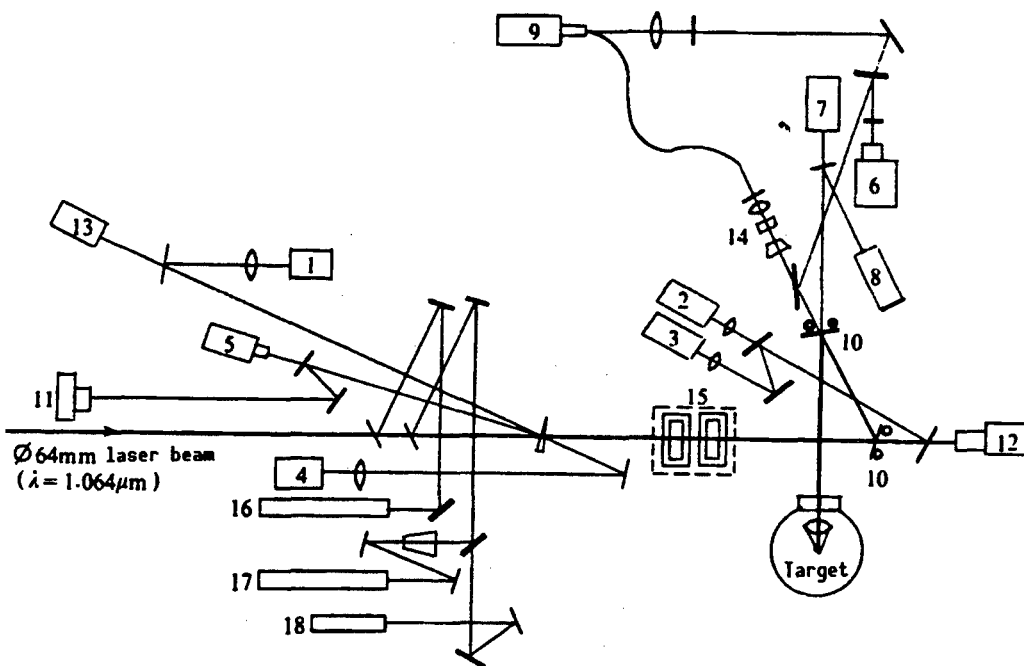


Figure 1. Layout of Optics of the Frequency-Doubling System

Key: 1. Fundamental-frequency laser energy calorimeter; 2. Frequency-doubled laser energy calorimeter; 3. Residual fundamental-frequency laser energy calorimeter; 4. Reflected laser energy calorimeter; 5. Fundamental-frequency laser beam far-field array camera; 6. Frequency-doubled laser far-field array camera; 7. Target location system; 8. Focus tuning transducer; 9. Streak camera; 10. Laser separation film ($\tau_{0.53} = 99.7\%$, $\tau_{1.06} = 99.0\%$); 11. Fundamental-frequency laser near-field camera; 12. Beam collimator; 13. SNR measurement system; 14. Streak-camera fundamental-frequency coupling system; 15. Frequency doubler; 16. Frequency-doubler collimating oscillator; 17. Focus tuning CW YAG frequency-doubling oscillator ($\lambda = 0.53 \mu\text{m}$); 18. He-Ne laser

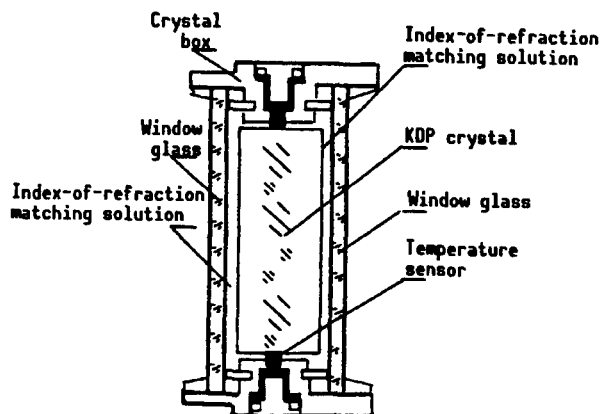


Figure 2. Frequency Doubler

high-precision two-dimensional servo rack (with $1''$ /step precision). In addition, a phase-matching optimization control system was developed to control the two-dimensional servo rack. An automatic mode-locked Q-modulated oscillator with output characteristics and frequency similar to those of the main laser is installed. By using special optics, the laser emitted by that oscillator is made precisely co-axial with the main laser in order to ensure the accuracy of adjustment. Optimal

phase matching of the crystal is achieved by adjusting the phase-matching angle of the crystal and using the light-intensity ($I_{2\omega}/I_{1\omega}$) comparison method with the high-precision two-dimensional servo rack and the optimization control system.

3. Measurement System

The laser parameters to be measured include energy of fundamental-frequency incident laser, energy of frequency-doubled laser, energy of remaining fundamental-frequency laser, far-field divergence angles for fundamental-frequency and frequency-doubled light, near-field distribution, and pulsewidths of fundamental-frequency light and frequency-doubled light. The simultaneous measurement of energy for fundamental-frequency, frequency-doubled, and remaining fundamental-frequency light requires monitor the energy balance in order to ensure the accuracy of measurement. Figure 3 shows a layout of the measurement system.

4. Automatic Thermostatic System

In order to improve the stability of energy output and quality of the frequency-doubled laser, the crystal must operate in a constant temperature and humidity environment (Δ^t is equal to or less than $\pm 0.2^\circ\text{C}$). To this end, an automatic constant-temperature control system was developed. The frequency doubler is placed in a constant

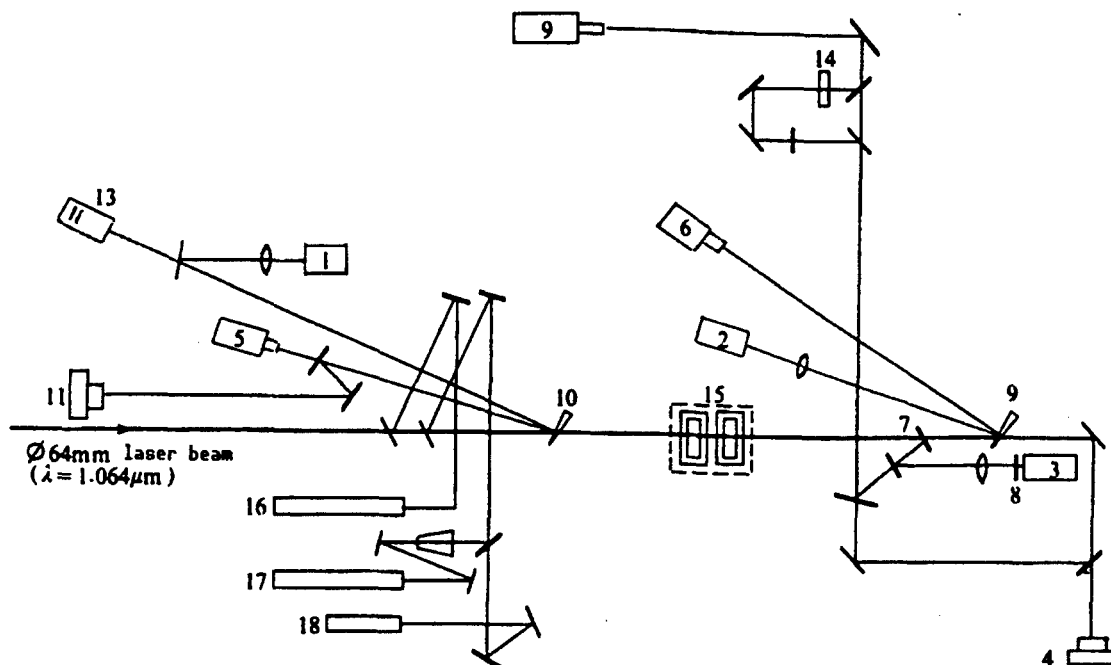


Figure 3. Frequency-Doubler Measurement System

Key: 1. Calorimeter for fundamental-frequency light; 2. Calorimeter for frequency-doubled light; 3. Calorimeter for remaining fundamental-frequency light; 4. Near-field array camera for frequency-doubled light; 5. Far-field array camera for fundamental-frequency light; 6. Far-field array camera for frequency-doubled light; 7. Laser separation film ($r_{1.06} = 100\%$, $\tau_{0.53} = 88\%$); 8. $0.53\mu\text{m}$ absorption glass; 9. Streak camera; 10. Light reflector; 11. Near-field camera for fundamental-frequency light; 14. Optical path delay system; 15. Frequency-doubling system

Table 1. Results of Matching Fluids

Matching fluid	FL-G35	FL-G5	ZP-2
Index of refraction n_n	1.390	1.385	1.280
Absorption coefficient α (cm ⁻¹)			
Wavelength			
266 (nm)	0.0364	0.1583	0.2275
355 (nm)	0.0036	0.0117	0.0264
532 (nm)	0.0052	0.0389	0.0036
1064 (nm)	0.0154	0.0227	0.0048

temperature box and heated by infrared lamps. The temperature on the surface of the crystal is measured by a thermistor (see Figure 2). Heating is controlled by a controller to maintain the crystal at approximately 4°C above room temperature. Temperature fluctuation is kept equal to or less than +/-2°C to ensure stability.

III. Technical Issues Concerning the Development of the Frequency-Doubling System

1. Selection of Crystal

A frequency-doubling crystal is a nonlinear optical material which generates the frequency-doubled light. Its quality directly affects the conversion efficiency of the process and quality of the resulting light. Different crystals produce drastically different harmonic waves on different lasers. The KDP crystal has a high nonlinear coefficient. It is easier to grow and process a large high-quality piece. Furthermore, it is relatively transparent in the visible and near infrared. It has a relatively high threshold against light damage. Hence, this crystal is very suitable as a frequency-doubling material for high-power lasers. Presently, KDP crystals are often chosen as the nonlinear optical material for harmonic wave conversion in high-power Nd-glass lasers in other countries.

Based on the characteristics of the LF-11 laser apparatus and the frequency-doubled data obtained, KDP crystal was chosen as the nonlinear optical material for the frequency-doubling system. The crystal parameters are as follows:

Crystal matching mode	Type II, critical phase matching
Crystal size	70 mm diameter x 16 mm thick and x 14 mm thick
Effective nonlinear coefficient	$d_{\text{eff}} = 0.557 \times 10^{-12} \text{m/V}$
Transparent band	0.2-1.5 μm
Light-resistant threshold	$> 5.5 \text{ GW/cm}^2$
Index of refraction	1.06 μm , $n_0 = 1.4942$, $n_e = 1.4602$
	0.53 μm , $n_0 = 1.5131$, $n_e = 1.4711$
	0.35 μm , $n_0 = 1.5320$, $n_e = 1.4866$

Absorption coefficient	1.06 μm , $\alpha = 2 \times 10^{-2} \text{cm}^{-1}$
	0.53 μm , $\alpha = 4 \times 10^{-4} \text{cm}^{-1}$
	0.35 μm , $\alpha = 1 \times 10^{-3} \text{cm}^{-1}$
Axis fixing error (phase matching precision)	$< 5''$
Machining precision of optics	$N = \lambda/2$, $\Delta N = \lambda/4$, ($\lambda = 5320$ Angstroms)

2. Selection of Index of Refraction Matching Fluid

In order to avoid deliquescence of crystal in air and effectively minimize Fresnel reflection loss at the end, the crystal is sealed inside a box filled with a fluid of matching index of refraction (see Figure 2). Therefore, laser absorption and light intensity threshold of fluid and the degree of matching between the fluid and the window will have a direct impact on the conversion efficiency and safety of the frequency doubler. It is desirable to choose a nonaqueous fluid with minimum absorption and an index of refraction and absorption coefficients of three fluids and the results are shown in Table 1. A comparison was made and the best one was selected.

After taking the test results into consideration, although FL-G35 has an index of refraction very close to the crystal and glass and has the least absorption coefficient, it is too concentrated. It is very difficult to use because it traps too many bubbles in the oil layer and does not flow easily. This will adversely affect the quality of the frequency-doubled light. ZP-2 has a low index of refraction which causes a higher Fresnel reflection loss at the end. Although the light absorption coefficient for FL-G5 is relatively low, the oil layer in assembly is very thin (0.2-0.5 mm). Therefore, from an overall perspective and based on experimental data, FL-G5 appears to be a more practical fluid.

3. Development of Laser Film

The laser film is a key issue in harmonic wave conversion. After passing through the nonlinear crystal, different frequencies are mixed together and must be separated. Nevertheless, the quality of the beam must not be adversely affected. Furthermore, as the wavelength gets shorter, the damage-resistant threshold will be lowered.² This is a tough issue in a high-power laser. Therefore, it

is of vital importance to develop high-intensity, high-quality laser separation films for frequency doubling. Based on our specifications and experimental needs, a series of laser films was jointly developed with the CAS

Institute of Optoelectronic Technology. The films' light damage-resistance thresholds were tested and the results are shown in Table 2. Basically, the requirements for frequency-doubling experiments have been met.

Table 2. Measured Laser Damage-Resistance Thresholds

Number	Film	Film system	Number of layers	Wavelength (m)	Damage threshold (GW/cm ²)
2	0.53 μ m HR	Ti ₃ O ₅ + SiO ₂	17	0.53	3.17
3	0.53 μ m HR	HfO ₂ + SiO ₂	19	0.53	18.20
6	1.06 μ m HR	Ti ₃ O ₅ + SiO ₂	18	1.064	17.11
9	1.06 μ m HT	Al ₂ O ₃ + MgF ₂	2	1.064	16.20
11	0.53 μ m HT	ZrO ₂ + HgF ₂	2	0.53	14.60
7	1.06 μ m HR	Ti ₃ O ₅ + SiO ₂	20	0.53	2.50

4. Development of Optimum Phase-Matching Control System

In the critical phase-matching mode, precision adjustment of the phase-matching angle is the premise for achieving high-efficiency frequency doubling. Theoretical analysis shows frequency-doubling efficiency drops rapidly with increasing mismatch of the phase angle. When mismatched, the frequency-doubling conversion efficiency fluctuates with the incident fundamental-frequency laser intensity.⁹ This will make it very difficult to operate the laser and to conduct the experiment. To this end, a control system was developed to optimize phase matching. The system compares the intensity of the incident fundamental-frequency laser to that of the frequency-doubled laser and automatically fixes the orientation of the crystal using a "mountain climbing" method to lock the matching-phase angle at the point of highest conversion efficiency. The mismatch angle $\Delta\theta$ will approach minimum. Figure 4 shows the principle of the control system.

A fully automatic mode-locked, Q-modulated 1-Hz-prf pulse oscillator, similar in characteristics to the main

laser, was used. Its optical axis was adjusted to coincide with that of the main laser. The energy of the fundamental-frequency laser and that of the frequency-doubled laser were measured and processed by a microcomputer to calculate the conversion efficiency $I_{2\omega}/I_{1\omega}$. Every value is compared to the previous one to make corrections. The controller controls the servo rack based on this correction signal. A variable-step control algorithm is employed. Figure 5 shows the control-program flow-chart. Because of this optimization control system, the accuracy of phase matching is significantly improved. The operation of the entire system totally meets the experimental requirements.

IV. Experimental Results

During the tuning of the frequency-doubling system, experiments were done with 70-mm diameter x 14 mm and 70-mm diameter x 16 mm crystals. Results were obtained. The optics are shown in Figure 3.

1. Conversion Efficiency

Frequency-doubling conversion efficiency experiments were done with 14-mm thick and 16-mm thick KDP

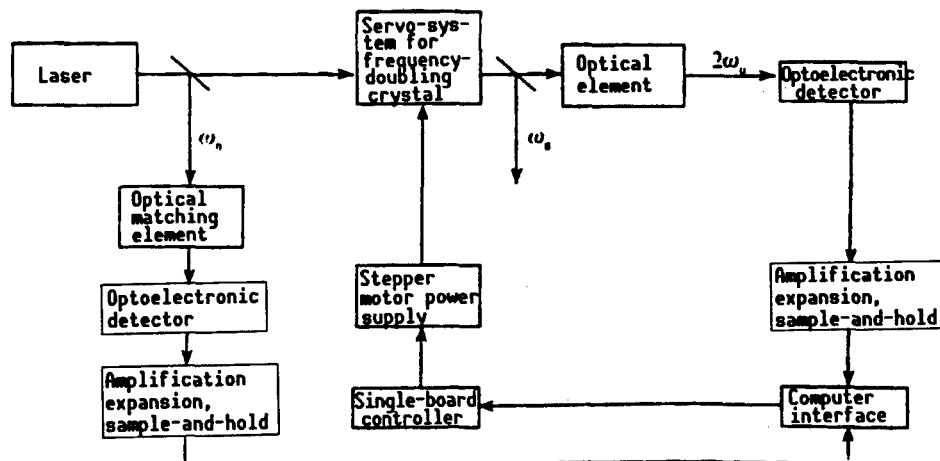


Figure 4. Principle of the Control System to Optimize Phase Matching

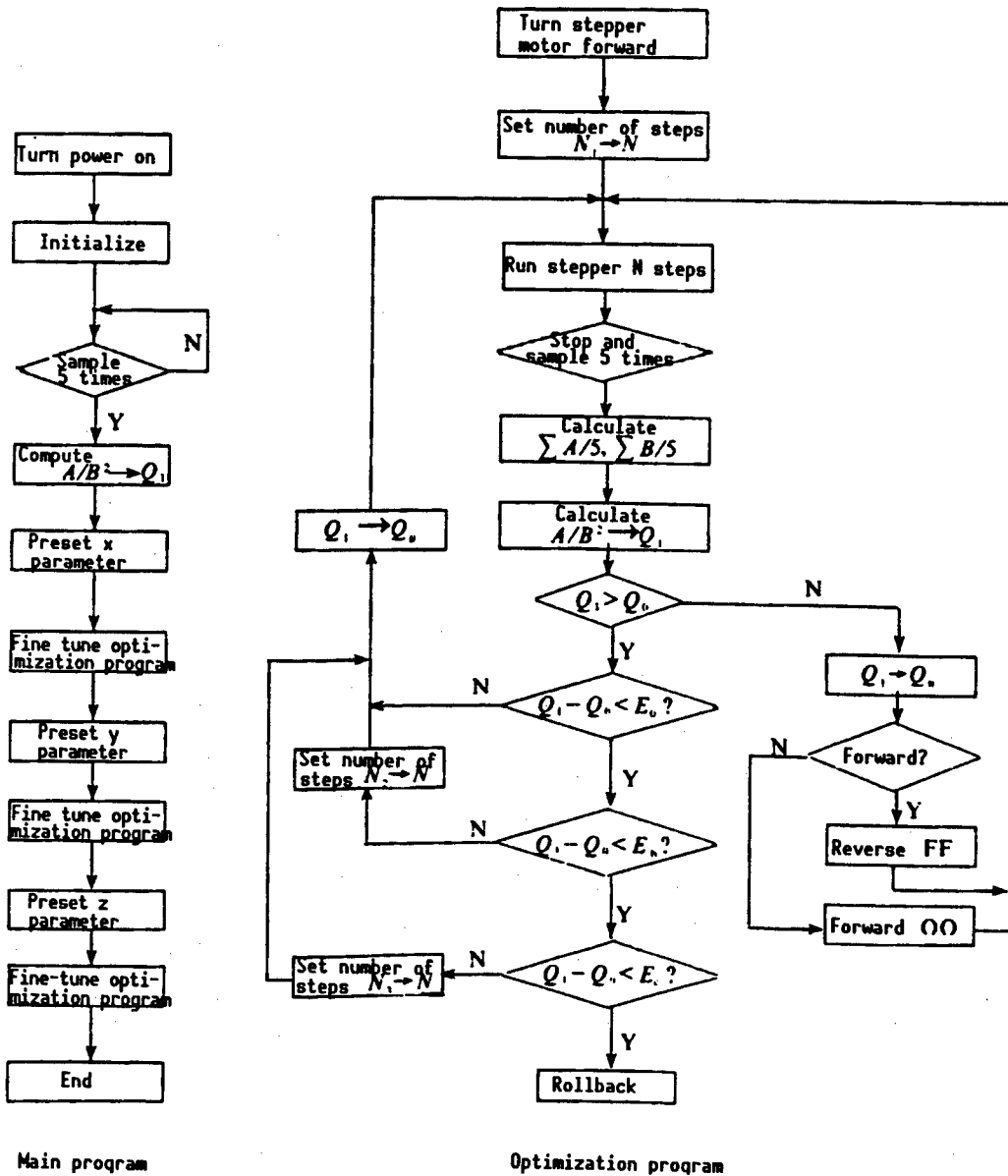


Figure 5. Flowchart of the Control Program To Optimize Phase Matching of the Frequency-Doubling Crystal

crystals. Three Apollo laser energy calorimeters were used. Apollo (1) is used to measure the fundamental-frequency incident laser energy $E_{1\omega}$. Apollo (2) is used to measure the energy of the frequency-doubled laser $E_{2\omega}$ and Apollo (3) is used to measure the energy of the residual fundamental-frequency light $E_{1\omega}$. The relative measurement error is <3 percent. The three measurements are balanced to ensure the reliability of the measurement. The experimental results are shown in Table 3.

Table 3. Conversion Efficiency of Frequency-Doubling

KDP crystal size	Fundamental-wave intensity (GW/cm ²)	η_{ext} (%)*	η_{int} (%)**	Conversion loss (%)
ϕ 70 x 14 mm	1.11	68.4	75.2	9.2
ϕ 70 x 16 mm	0.81	62.9	72.1	12.7

* External energy conversion efficiency $\eta_{ext} = E_{2\omega}/E_{1\omega}$

** Internal energy conversion efficiency $\eta_{int} = E_{\omega}/(E_{2\omega} + E_{1\omega})$

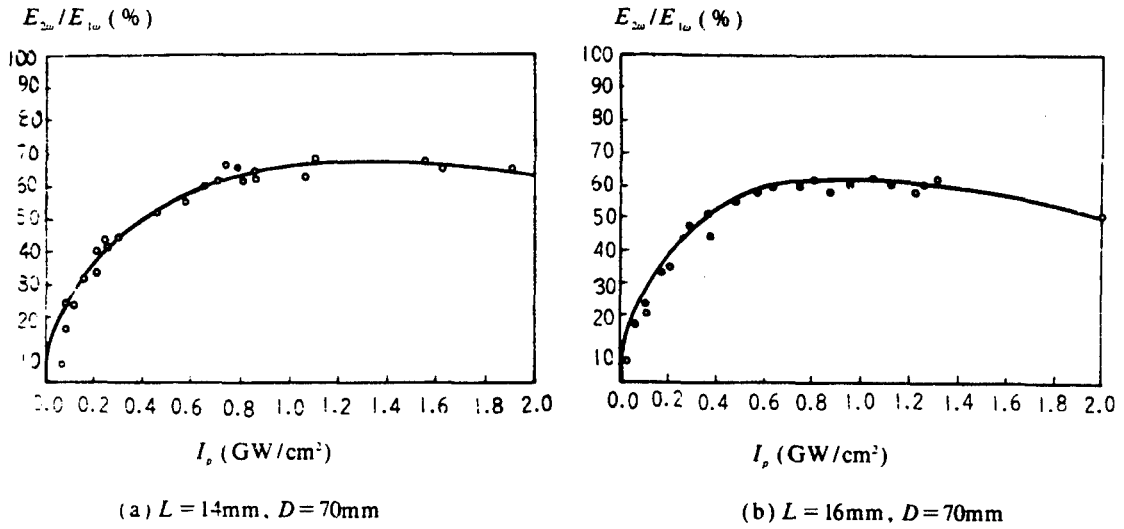


Figure 6. Characteristic Curves for KDP Crystals (Type II)

In addition, when the fundamental-frequency laser power density $I_p > 0.4 \text{ GW/cm}^2$, the external energy conversion efficiency of the two crystals may be over 50 percent. Good agreement is found between experiment data and calculated values.¹ Figure 6 shows the $\eta_{\text{ext}} - I_p$ curves for both crystals.

2. Tuning FWHM of Mismatch-Phase Angle

The tuning full width at half maximum (FWHM) of mismatch angle of the same crystal is determined by its length.⁹ The longer the crystal is, the shorter the tuning FWHM becomes, and the more difficult it is to achieve phase matching. However, a short crystal requires a high

fundamental-frequency power density to achieve high-efficiency conversion. Therefore, the key to realizing high-efficiency frequency doubling is to choose a crystal of suitable length [i.e., thickness]. Based on theoretical analysis and earlier experimental data, 14 mm and 16 mm KDP crystals were selected for frequency doubling. The tuning curves for both crystals were obtained (see Figure 7). Our results show that when the incident fundamental-frequency power density $I_p = (0.85 \pm 20\%) \text{ GW/cm}^2$, the tuning FWHM of the 14-mm KDP crystal is $\Delta\theta_{\text{FW}} = 2.01 \text{ mrad}$ and that of the 16-mm KDP crystal is $\Delta\theta_{\text{FW}} = 1.90 \text{ mrad}$. Furthermore, the accuracy of the control system for optimal phase matching was also evaluated. From Figure 7, we know that the system has an accuracy of 3 percent (rms).

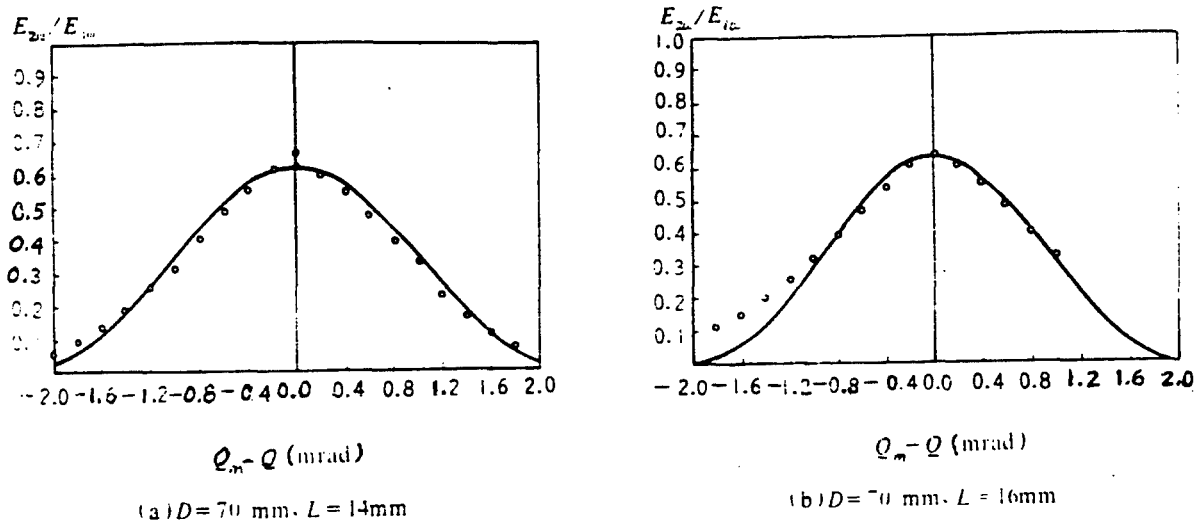


Figure 7. Tuning Curves for KDP Crystals (Type II)

3. Quality of Frequency-Doubled Beam

Far-field divergence angle is an important parameter for judging the quality of a light beam. Experimentally, an array camera is used to measure the far-field divergence angle and the results are shown in Table 4. It was found that the far-field divergence angle of the frequency-doubled beam is approximately 1.3 times larger than

that of the fundamental-frequency beam. The ability to focus the beam declines. Using an $f/3$ lens, the mean focal spot on the target is equivalent to 4.6 times the diffraction limit for the fundamental-frequency light. For the frequency-doubled light, however, it is equivalent to 11.4 times, or an increase of 2.5 fold [i.e., 250 percent].

Table 4. Far-Field Divergence Angles for $1\omega_0$ and $2\omega_0$ Laser Beams

Exp. number	Wavelength (m)	Divergence angle (mrad)	Focal-spot radius* (m)	N**	N_2/N_1
890919037	1.064	0.193	19.3	4.8	2.41
"	0.532	0.235	23.5	11.6	"
890920045	1.064	0.166	16.6	4.1	2.49
"	0.532	0.207	20.7	10.2	"
890920050	1.064	0.222	22.2	5.5	2.13
"	0.532	0.238	23.8	11.7	"
890920055	1.064	0.151	15.1	3.7	2.95
"	0.532	0.222	22.2	10.9	"
890921060	1.064	0.229	22.9	5.6	2.23
"	0.532	0.253	25.3	12.5	"
890921061	1.064	0.173	17.3	4.3	2.74
"	0.532	0.239	23.9	11.8	"
890921062	1.064	0.172	17.2	4.2	2.67
"	0.532	0.228	22.8	11.2	"

*Focal-spot radius on target surface, focal length of lens $f = 200$ mm.

**Multiples of lens diffraction limit.

This increase in far-field divergence angle leads to a decrease in the ability to focus the laser beam, a result not desirable for the experiment. This increase is primarily due to the precision of assembly of the frequency doubler. It is impossible to keep the optical axis of the entire KDP crystal consistent in the growth process. Its accuracy is approximately $5''$. Furthermore, the quality of the crystal material and purity of the refractance matching fluid also affect the quality of the beam. A minute amount of impurity in the crystal and fluid can cause diffraction which leads to an increase of far-field divergence angle of the frequency-doubled light. The quality of the laser beam is also affected by nonlinear effects.

4. Time Profile of $2\omega_0$ Laser

Theoretical analysis shows that the pulsewidth of higher harmonic waves generated by a nonlinear crystal will be compressed. To this end, a streak camera was used to measure the pulsewidths of light at $1\omega_0$ and $2\omega_0$. The result indeed shows that the frequency-doubled light is compressed. Figure 8 shows the time profiles of both fundamental-frequency and frequency-doubled light (890909289). When the incident fundamental-frequency light power density is 0.49 GW/cm², the pulsewidth of the $2\omega_0$ laser beam is compressed by a factor of 1.37

relative to that of $1\omega_0$ (i.e., $\tau_{p(2\omega)} = \tau_{p(1\omega)}/1.37$). Based on a great deal of data, the compression of $2\omega_0$ light becomes less significant with rising incident fundamental-frequency laser intensity. This is consistent with theoretical analysis.

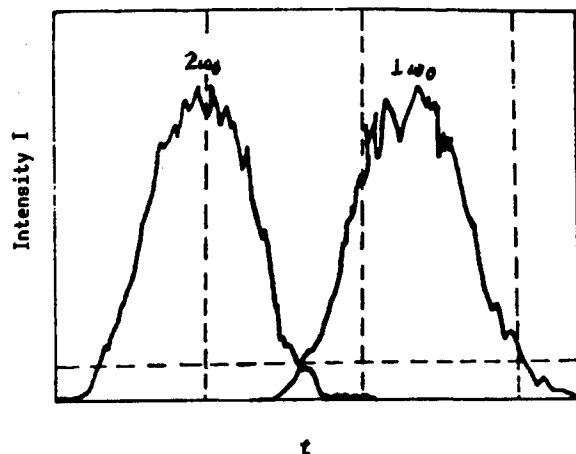


Figure 8. Time Profiles of $1\omega_0$ and $2\omega_0$ Laser Beams

References

1. W. Sekes, et al., IEEE J. QUANTUM ELECTRON, QE-17, No 9, 1981, p 1689.
2. J.S. Hetelum, et al., LLNL, Laser Program Annual Report, 1 (2-8), 1980, pp 2-225.
3. Takatomo Sasaki, et al., translated by Lu Qiaoqing [0712 0829 7230], GUOWAI JIGUANG [FOREIGN LASERS], No 1, 1988, p 21.
4. Cai Xijie [5591 1585 3381], et al., GUANGXUE XUEBAO [ACTA OPTICA SINICA], Vol 6 No 12, 1986, p 1898.
5. You Chenhua [1429 2525 5478], Lu Zukang [7120 4371 1660], et al., Ibid., Vol 6 No 5, 1986, p 413.
6. Fan Qikang [5400 3823 5478], et al., JIGUANG [LASER], Vol 6 No 3, 1979, p 14.
7. Cai Xijie, et al., GUANGXUE XUEBAO [ACTA OPTICA SINICA], Vol 5 No 11, 1985, p 975.
8. Wei Xiaofeng, Zhang Xiaomin, et al., "Experimental Study of Large-Aperture High-Efficiency Frequency-Doubling With KDP Crystals," to be published.
9. Edited by Central China Polytechnical College, "Laser Technology," Hunan Science and Technology Publishing House, 1981, p 226.

Picosecond Soft X-Ray Streak Camera Described

91FE0588E Chengdu QIANG JIGUANG YU LIZI SHU [HIGH-POWER LASER AND PARTICLE BEAMS] in Chinese Vol 3 No 1, Feb 91 p 127

[Article by Gu Boxun [7357 0130 8113]: "Picosecond Soft X-Ray Image-Converter Tube Scanning Camera"]

[Text] Abstract: In laser nuclear fusion studies, the spectrum emitted by the high-temperature, high-density plasma produced by the imploded target is mainly in the soft X-ray region. The study of these soft X-rays involves a variety of plasma-related parameters including electron temperature, electron energy distribution, and different unstable states as a function of time. Nevertheless, the process of X-ray production is of the order of picoseconds and the diameter of the target irradiated by laser is merely 100 microns or so. Therefore, it is necessary to have X-ray diagnostic means with picosecond time resolution and micron-level spatial resolution. A soft X-ray picosecond image-converter tube scanning camera was developed to meet this need. It is an X-ray band detector/analyzer with the highest time resolution. Moreover, it has a very high spatial resolution. In conjunction with an X-ray spectrometer, it is a

camera capable of recording instantaneous X-ray spectrum. Together with an X-ray pinhole camera, it is possible to determine one-dimensional spatial resolution as a function of time.

This camera is primarily comprised of an X-ray scanning image-converter tube, scan control circuit, image enhancer and its power supply, and image recording system. The substrate of the narrow cathode of the image-converter tube is made of 1000 angstrom C_3H_8 thin film which is highly transmissive to soft X-rays. The cathode is made of gold or cesium iodide with a conductive base. The image-converter tube is a flat cathode plane grid image converter. The image enhancer is an inverted image electronic enhancer with microchannels. The contact camera puts the film immediately against the fiber-optic output window of the image enhancer to record the event.

Major Specifications of the Camera

- Limiting time resolution: The full width half maximum (FWHM) of the X-ray streak image determined using an X-ray filter method and the FWHM of the streak image obtained using 8-ps laser pulses are both under 50 ps.
- Scanning resolution of the camera: Greater than 8 line pairs/mm.
- Static spatial resolution: 20 line pairs/mm.
- Wavelength response: 0.1-10 keV.
- Effective dimensions of slit cathode: 30 μm x 12 mm, 50 μm x 12 mm, and 100 μm x 12 mm.
- Scanning rate: 76 ps/mm, 100 ps/mm, 200 ps/mm, and 360 ps/mm.
- Dynamic range of the camera: Greater than 30.
- Delay time: 15.35 ns.
- Trigger flutter: +/-150 ps.
- Scan linearity: less than 8 percent.

The Xian Institute of Optics and Fine Mechanics of the Chinese Academy of Sciences developed this soft X-ray picosecond image-converter tube scanning camera in 1986 by combining advanced technologies such as modern physics, optoelectronics, fine mechanics, and electronics. It was then further improved to become an instrument. In 1989-1990, it was officially used to measure the X-ray spectra of plasmas generated by laser-irradiated targets at the joint laboratory of SIOFM and CAEP. In addition, various performance characteristics of the camera were experimentally evaluated. It has been proven that the camera has excellent reliability and reproducibility. Various characteristics such as overall interference resistance, image quality, trigger flutter, and dynamic spatial resolution are at the same advanced level as those of similar [foreign-made] instruments made in the 1980's. It has played an important role in the exploration of physical phenomena in the leading edge of science and has yielded a number of good results.

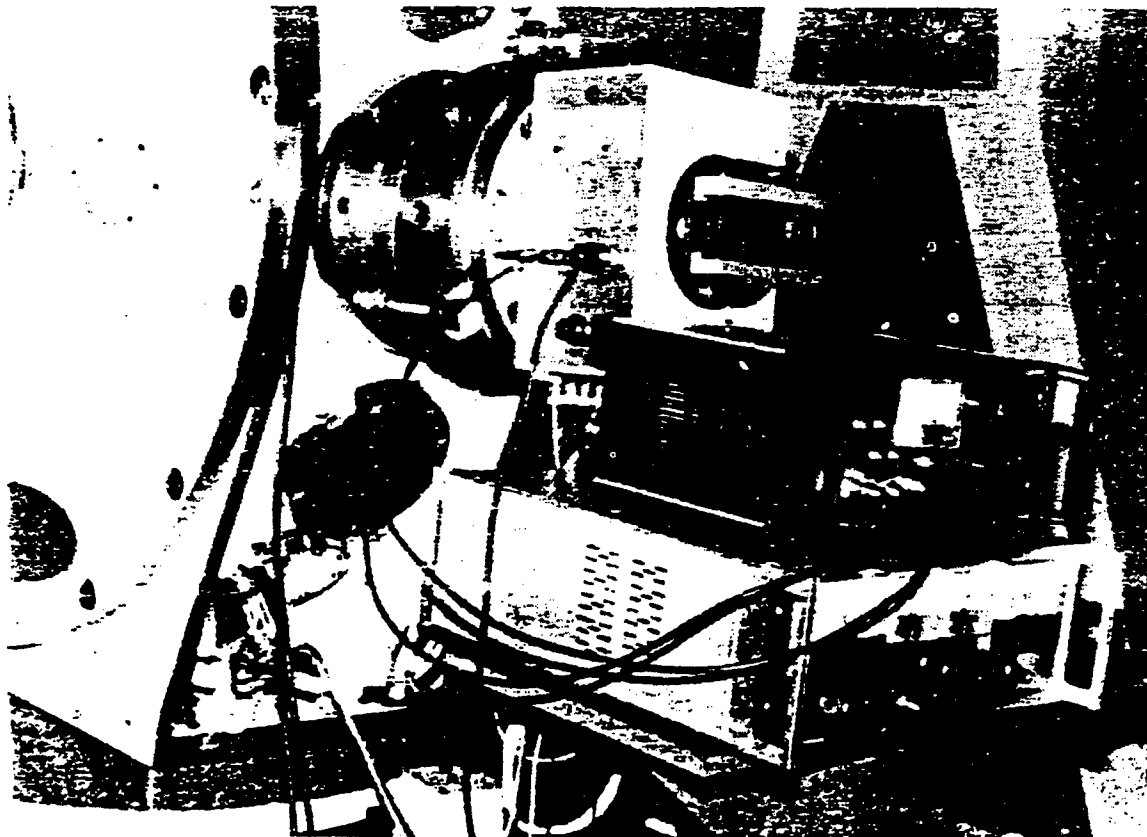


Photo caption: Domestically made soft X-ray scanning camera and plane-focal-field grating spectrograph installed side-by-side to perform X-ray laser diagnostic tests in the LF-12 target chamber [photograph from Chengdu QIANG JIGUANG YU LIZI SHU, Vol 2 No 4, Nov 90, inside front cover].

ICF, X-Ray Laser Experiments With LF-12 (Shen Guang) Apparatus Described

91FE0588F Beijing RENMIN RIBAO in Chinese
3 May 91 p 3

[Article by Xiao Guan'gen [5618 7070 2704]:
"Advanced Experimental Results With 'Shen Guang'"]

[Text] The LF-12, a high-power laser apparatus named "Shen Guang" ["Magic Light"], has been in full-load operation for three years and has produced a number of first-class experimental results. This accomplishment was given the 1990 national first-class technical progress award.

The "Shen Guang" was developed by CAS's Shanghai Institute of Optics and Fine Mechanics (SIOFM). It is the largest high-power neodymium-glass laser apparatus in China and is one of a handful of such installations in the world.

The "Shen Guang" is composed of a laser system, target range system, measurement and diagnostic system, and laboratory environmental engineering system. This apparatus can focus the high-power laser beam to an

0.1-mm point or a fine line by using lenses. When this light is shined upon materials in certain special forms (called targets), it is capable of instantaneously resulting in thousands of degrees of high temperature and thousands of atmospheres of high pressure to produce dense plasmas. This effect can be used to study many important physical problems such as thermonuclear fusion, X-ray lasers, and high-pressure shockwaves. The total power output of "Shen Guang" is of the order of 1 billion kilowatts (kW). Its high-precision target system is capable of handling 0.1-mm microsphere targets, black-hole targets, step targets, and a variety of X-ray laser targets. Furthermore, it can operate in the single-beam, dual-beam, and combined dual-beam modes.

When the apparatus passed national appraisal in 1987, experts believed that its overall technical performance had reached the same advanced level as that of other comparable units abroad; this signified that China had become one of a few countries capable of developing such a high-power laser apparatus.

Following appraisal, the problem was to keep the apparatus in stable operation. Scientists at SIOFM and the China Academy of Engineering Physics (CAEP) jointly formed a "high-power laser physics laboratory" and organized technical people to make 10 technical

improvements on the four major systems. Moreover, an overall maintenance was performed to significantly improve its stability and reliability. The overall performance of the device is considerably better than that at the time of appraisal and is at an all-time high. In addition, a new line-focusing system has been developed to meet new experimental requirements to expand the capability of the device.

After a great deal of solid effort, the "Shen Guang" has been transformed from a research tool to an advanced practical device. It is capable of undertaking demanding physical experiments in basic research.

For over three years, the "Shen Guang" has been operating in a saturated state. A total of more than 2,500 beams have been emitted, for an average of over 800 beams per year. This kind of high usage rate is comparable to any advanced laboratory in the world.

Since it was put in operation, this facility has been made available to numerous research institutions in China. A number of high-level experimental results have been obtained to date. CAEP has conducted a series of inertial-confinement fusion experiments with the "Shen Guang." Not only apparent compression and high-level neutron production were observed with deuterium and tritium targets in the direct-drive mode, but also the regularity of a series of physical processes was investigated in the indirect-drive mode. In particular, high-radiation temperature and neutron output were found with a black-hole target. This discovery is a significant milestone and of advanced world-class level. In addition, they also generated excellent planar shockwaves to measure the equation of states of a material at high pressure from a step target by taking advantage of the uniformly focused laser beam from the "Shen Guang." The accuracy of measurement is better than that with a similar device elsewhere in the world.

In X-ray laser research, the CAEP technical staff obtained the output of five soft X-ray lines from neon-like germanium, which is also a world-class accomplishment. On this basis, they achieved the series amplification of X-rays with a unique "butt-joined twin-target" approach. The overall gain is several million fold, which puts them in the lead in the world.

The SIOFM technical staff conducted recombination X-ray laser experiments on the "Shen Guang" and obtained outstanding results. For the first time, they obtained four new X-ray lines with Li-like silicon; wavelength is below 100 angstroms. This helps push the X-ray laser toward shorter wavelengths.

The successful development of the "Shen Guang" is a milestone in high-power laser technology in China. This is because its power is of the order of 1 billion kW and a device at this level plays a key role in this field in any country of the world.

Additional Note on LF-12 Apparatus

91FE0588G Beijing RENMIN RIBAO in Chinese
3 May 91 p 3

[Article by unnamed author: "LF-12 Experimental Apparatus"]

[Text] The LF-12 ("Shen Guang") is a laser apparatus developed by Deng Ximing [6772 6932 6900], Yu Wenyan [0151 2429 3508], Fan Dianyuan [5400 3329 0337], Hu Shaoyi [5170 4801 5902], and Huang Zhenjiang [7806 6966 3068] of CAS's SIOFM. Because its high-peak-power output is 2×10^{12} W, it is named LF-12.

The "Shen Guang" is a huge high-power laser system consisting of hundreds of optical devices. Through a dozen stages of amplification, its instantaneous output power can reach as high as 1 billion kW. This is several times higher than the power generating capability of the entire country. However, the light only lasts one billionth to one ten-billionth of a second. Such an intense beam is first highly focused by lenses and then shines on an 0.1-mm diameter spherical target. The temperature rises to tens of millions of degrees and the pressure builds up to several thousand atmospheres to allow nuclear fusion to take place. This results in the release of energy millions of times higher than that of the corresponding chemical reaction. This kind of large, sophisticated precision laser system is only available in a few other countries, such as the United States and Japan.

The majority of components in the "Shen Guang" was successfully developed in China. The process, taking seven years from development to appraisal, involved 15 innovations in advanced technology. A few of them are considered unique worldwide.

The "Shen Guang" provides the means to conduct laser nuclear fusion experiments. In addition, it can be used in high-power laser/plasma research which is a leading-edge science. In 1988, the "Shen Guang" was named the main experimental apparatus for X-ray laser research in the national high-technology plan.

High-Power Nd:YAG Laser With Variable Pulsewidth

91FE0626A Shanghai GUANGXUE XUEBAO [ACTA OPTICA SINICA] in Chinese Vol 11 No 5, May 91
pp 413-418 [MS received 6 Sep 90, revised 25 Oct 90]

[Article by Lin Lihuang [2651 4409 3552], Ouyang Bin [2962 7122 2430], Kang Yuying [1660 3768 5391], Ge Wen [5514 2429], and Chen Shisheng [7115 2514 0524] of the Shanghai Institute of Optics and Fine Mechanics (SIOFM), Chinese Academy of Sciences, presented at CLEO'90 and supported by the National Natural Science Foundation: "High-Power Nd:YAG Laser With Variable Pulsewidth"]

[Text] Abstract: The structure and performance of a two-stage Nd:YAG compact high-power laser system are described. It consists of three major components: an

active-passive colliding-pulse mode-locked (CPM) oscillator, a single-pulse selector, and a four-pass amplifier. The oscillator generates a train of mode-locked pulses with an envelope fluctuation of $< \pm 4$ percent. The pulsewidth can be conveniently adjusted over a wide range (20 ps - 2.5 ns). For a single 0.1 mJ, 200 ps pulse, the four-pass filter can achieve an amplification factor of 7×10^2 .

I. Introduction

In the study of mutual interaction between lasers and materials, laser-induced nuclear fusion and X-ray lasers, the laser pulsewidth is required to vary from picoseconds to nanoseconds due to different target requirements. Laser pulses spanning such a wide range are traditionally provided by several laser oscillators operating in different modes (such as mode-locked, Q-modulated, pulse-shaped, etc.).

This paper reports the structure and output characteristics of a compact high-power Nd:YAG laser system. It consists of active-passive CPM Nd:YAG laser, a single-pulse selector (Pockels electrooptical switch), and a Nd:YAG amplifier. The amplifier and a few optical elements form a four-pass amplifier. The oscillator has a very high output stability. The envelope fluctuation of the mode-locked train of pulses is $< \pm 4$ percent. Furthermore, based on demand, the pulsewidth can be conveniently varied over a range of 20 ps to 2.5 ns. The four-pass filter can effectively amplify the chosen small signal.

II. Laser System and Output Characteristics

1. Active-Passive CPM Laser

Siegman¹ first presented the use of a laser cavity within an antiresonant ring in a solid-state laser to achieve CPM operation. Since then, a great deal of significant progress has been made. A study done by the authors² shows that colliding pulse mode-locking is a better passive mode-locking way of operation. It can establish an instantaneous particle distribution grating³ in a saturable absorber and has a stabilizing and pulse-compressing effect. However, the amplitude stability of a CPM solid-state laser is still much lower than that of an active-passive mode-locked solid-state laser⁴ and cannot meet certain requirements in use.

In the CPM Nd:YAG laser used in this experiment, an acousto-optic modulator (AOM) was added to achieve active-passive CPM operation. Experimental results show this mode of operation has the advantages of both mode-locking methods mentioned above. In particular, photochemically stable saturable absorbers that are difficult for mode locking because of long relaxation time, such as BDN dye (nickel di(4-dimethyl dithio diacetophenone))⁵ and color-center crystals (such as specially doped YAG crystals like Cr:Nd:YAG,⁶ and lithium fluoride crystals like LiF:F₂⁻⁷), are able to operate stably to provide mode-locked output.

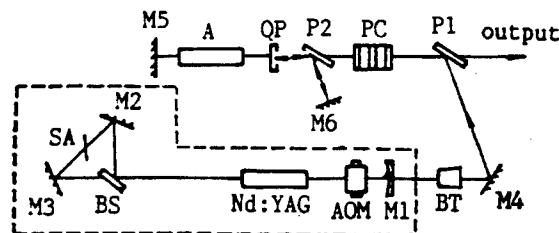


Figure 1. Schematic of the Laser System

The dotted block in Figure 1 shows an active-passive CPM laser. It is driven at 50 MHz (RF). An AOM made of fused quartz (using lithium tungstate as the transducer) is located near the output mirror M1 to provide active amplitude modulation. The output cavity mirror is a concave mirror (with a radius of curvature of 10 m and a 50 percent reflectance at 1064 nm). Its flat side has an antireflective (AR) coating. The beam splitter, BS, of the antiresonant ring has a near 50/50 reflection-to-transmission ratio for s-polarized component at 45° incidence. The working medium is a 4-mm diameter, 65-mm long Nd:YAG rod. Both ends have an AR coating. It is placed in a double-ellipse cavity and is pumped with two straight xenon lamps. The saturable absorber, SA, is located at the center of the antiresonant ring.

Different saturable absorbers (with different relaxation times) of different transmissivities have been used in this work, including dichloroethane solution of pentamethyldiene (circulating), BDN dye film (polyester film with BDN), Cr:Nd:YAG crystal and LiF:F₂⁻ crystal. The mode-locked pulses generated by these absorbers have a pulsewidth range from 20 ps - 2.5 ns (not continuous). Specific saturable absorbers may be tested, labeled, and calibrated for optical path and then secured on a special mechanical structure to make it convenient to replace them rapidly in the antiresonant ring in order to be able to switch to a train of pulses with predetermined pulsewidth.

After the train of pulses is captured by a fast photodiode, it is displayed on a high-speed oscilloscope. The single-pulse selector picks a pulse and its full width at half maximum (FWHM) is measured with a streak camera. Considering the fact that the spectral response of the streak camera in the laboratory is between ultraviolet and visible, the 1064-nm visible, the 1064-nm light pulses first pass a KDP-crystal frequency doubler to become 532-nm pulses before entering the slit of the streak camera. From the shape and half width of the 532-nm pulse measured with the streak camera, it is possible to obtain the actual FWHM of the 532-nm pulse, Δt_s , by subtracting the intrinsic time expansion of the camera from the measured value. Then, the actual FWHM of the 1064-nm pulse, Δt , can be derived. Assuming the pulse shape is Gaussian, $\Delta t = (2)^{1/2} \Delta t_s$. In order to ensure that the factor $(2)^{1/2}$ is correct, it is required that the 1064-nm pulses be small signals in order to avoid other nonlinear effects. Moreover, the

KDP crystal should be at its optimal matching incidence angle with respect to the laser.

Experimentally, the following mode-locked trains of pulses have been obtained:

- 20 ps - 60 ps (using pentamethylidene dye solution)⁸
- 150 ps - 800 ps (using BDN dye film)

- 600 ps - 1.3 ns (using Cr:Nd:YAG color-center crystal)
- 2.0 ns - 2.5 ns (using LiF:F₂⁻ crystal)

Figure 2 shows typical oscillograms of mode-locked pulse trains from the oscillator when using the four absorbers described above, together with their corresponding second-harmonic streak-camera traces.

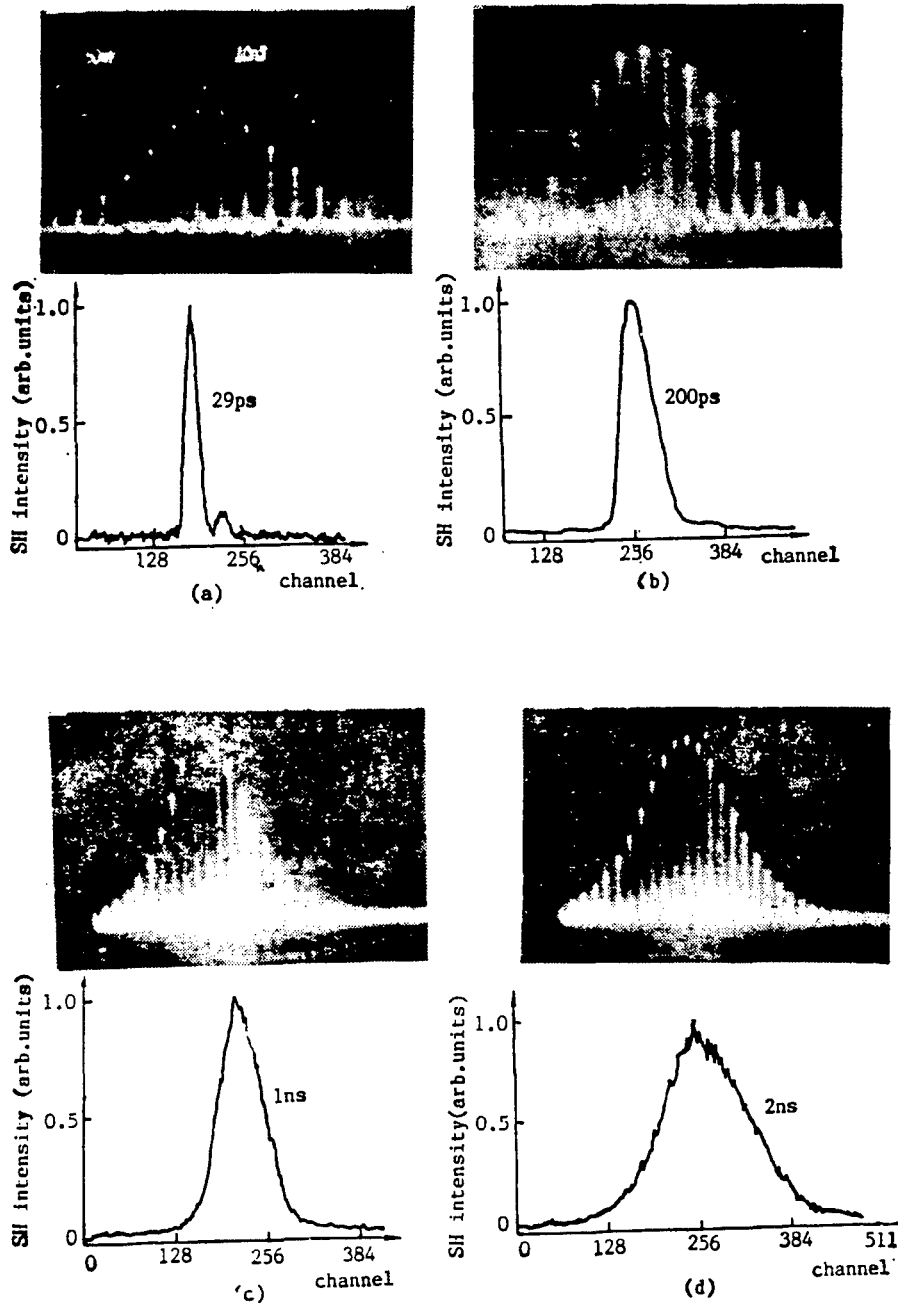


Figure 2. Oscillograms of Pulse Trains (Top, all periods between adjacent pulses are 10 ns), and Their Corresponding Streak Camera Traces at Wavelength of 532 nm (Bottom) for the Different Saturable Absorbers

Key: (a) pentamethylidene dye ($T = 40\%$), (b) BDN dye film ($T = 35\%$), (c) Cr-Nd:YAG color center crystal ($T = 22\%$), and (d) LiF:F₂⁻ color center crystal ($T = 45\%$). The deduced pulsewidths (FWHM) of 1064-nm laser pulses are marked in the figures, respectively.

It was found experimentally that the laser background on both wings is very clean because of using this active-passive CPM method. The output light is linearly polarized in the s-direction. Without a mode-selection grating, the laser cavity can output in the single transverse TEM₀₀ mode.

2. Four-Pass Amplifier

In reality, the energy of the single pulse chosen by the single-pulse selector is often very low, approximately 0.1 - 1 mJ. It needs multiple stages of amplification for actual use. Traditionally, light pulses pass through an amplifier medium once in the form of a traveling wave. With a small input signal, one cannot extract nearly sufficient energy stored in the laser amplifier. It is a low-efficiency, high-cost mode of operation.

A coaxial four-pass traveling wave Nd:YAG laser was designed in this work. One can extract sufficient energy stored in the amplifier medium. It is easier to operate than a regenerative amplifier.⁹ The four-pass amplifier consists of a Pockels electrooptical switch, an Nd:YAG amplifier, and a few optical elements to guide the light, as shown in Figure 1. The pockels box has two longitudinal KD*P crystals, and an avalanche photodiode (APD) circuit¹⁰ provides a high-voltage electrical pulse (driven by half-wave voltage mode), approximately 10 ns wide. It is capable of reliably choosing a pulse from the train of pulses that is closest to the maximum before the envelope reaches the highest level. After passing through a 1/4-wavelength plate, QP, the linearly polarized single pulse (assuming polarized in p direction) is converted into a circularly polarized pulse before entering the amplifier A. The light pulse amplified by the first pass of A is reflected by mirror M5 along the same optical path to be amplified by the second pass of A. This doubly amplified light passes through QP from the opposite direction and circularly polarized light is changed to linearly polarized light (in s-direction). It passes through P2 toward M and is reflected back along the same path. The beam then passes through QP to A to M5 to A to QP again. It is not only amplified two more times by A (which means it passes A a total of four times) but also changes its polarization from circular to linear (in p-direction). It passes through P2 to PC to P1. At this point, the electrooptical switch is still off, i.e., PC has no effect on the polarization of the light coming from the reverse directions; the light reaching polarizer P1 is still polarized in the p-direction. Consequently, it is transmitted completely through P1 (in the direction of the arrow shown in Figure 1).

In order to determine the properties of the four-pass amplifier, a 200-ps, 0.1-mJ pulse was chosen from the train of pulses emitted by the oscillator to be amplified. The amplifier is a 5-mm diameter, 63-mm long Nd:YAG rod. The output characteristics of the four-pass amplifier have been determined experimentally at different pumping energy levels and the results are shown in Figures 3 and 4. Figure 3 shows the gain G as a function of pass number at two different pumping energy levels

(52 J and 90 J). Our results indicate that the energy supplied by the four-pass amplifier is limited by the number of population-inverted particles at lower pumping energies. Its gain saturates easily. Only with sufficient pumping energy can a four-pass amplifier be fully effective. Figure 4 shows that the energy output increases linearly with rising pumping energy and four-pass amplification shows no sign of saturation. Therefore, to accurately operate a four-pass amplifier, the user must select the optimum pumping energy based on the energy and pulsewidth of the incident pulse and the characteristics of the amplifier (such as aperture and length). When pumped at 106 J, the pulse described above was amplified from 0.1 mJ to 75 mJ, corresponding to an amplification factor of 7×10^2 .

III. Discussion

(1) Using an active-passive CPM mode, not only ensures the stability and reproducibility of a mode-locked train of pulses, but also makes it possible to use saturable absorbers which cannot be used for mode-locking due to long relaxation time to obtain steady mode-locked output. When the power supply to the electrooptical switch shown in Figure 1 is shut off, it becomes a passive CPM laser. Pentamethyldiyne dye could be used as an absorber as reported in reference [2]. However, the stability of the amplitude of the output train of pulses deteriorates considerably with BDN and color-center crystals. With LiF:F₂⁻ crystal, it is sometimes impossible to obtain a totally modulated output. When the saturable absorber is removed from the antiresonant ring and placed near the output mirror M1, it becomes an active-passive mode-locked scheme similar to a F-P (Fabry-Perot) cavity (AOM driver turned on). Although the stability of the mode-locked output remains unchanged,

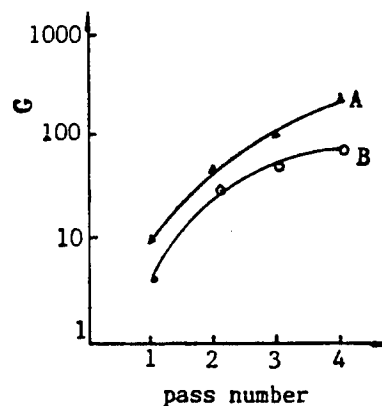


Figure 3. Amplification of the Four-Pass Amplifier for 0.1 mJ Input in 200 ps Pulsewidth as a Function of Pass Number Under Different Pump Energy (A-52J and B-90J)

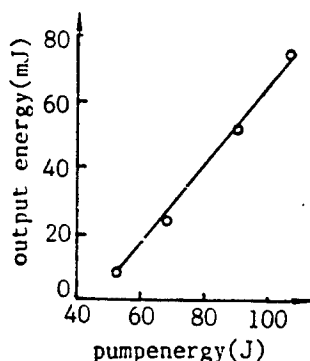


Figure 4. Output Energy From the Four-Pass Amplifier as a Function of Pump Energy for an Input Pulse Energy of 0.1 mJ With 200 ps Duration

our streak-camera traces nevertheless show that pulse-width was widened and there is a serious pulse-splitting effect (with the four saturable absorbers). This is particularly apparent with BDN thin film and color-center crystals.

Hence, the active-passive CPM scheme is capable of enhancing pulse discrimination and compression to yield a narrow and better pulse than a conventional cavity¹; possibly it can establish an instantaneous grating in the absorber and create a four-wave frequency-mixing effect.

(2) The four-pass amplifier can effectively amplify a low-energy weak pulse. However, with a long-pulsewidth, high-energy pulse, it saturates easily. To this end, the amplifier can be easily converted into a two-pass amplifier (by removing QP and M6 with output still pointing in the direction of the arrow, or by removing M6 with output pointing toward M6), based on the input pulse. Or, it may be converted into a single-pass amplifier (by removing M5, QP and either keeping or removing M6).

To operate in a working medium of even larger aperture, it is possible to realize four-phase amplification by using a large-aperture Pockels electrooptical switch or a Faraday magneto-optical isolator.

(3) The laser system described in this paper can be used as an independent high-power laser source. It may also be used as the front end of a larger-aperture Nd-glass laser apparatus to generate variable-pulsewidth seed pulses for amplification. The authors have also used phosphate-containing Nd glass as the working medium to repeat the work discussed above. Similar results have been obtained.

The authors wish to thank Professor Xu Zhizhan [1776 5267 1455] for his support and Yao Guangtao [1202 1639 3447] and Gui Youxi [2710 1429 0823] for supplying specially doped YAG.

References

1. A.E. Siegman, *OPT. LETT.*, Vol 6 No 4, July 1981, pp 334-335; A.E. Siegman, *PROC. SPIE*, Vol 322, 1982, pp 60-67.
2. Lin Lihuang, et al., *CHINESE PHYS. LETT.*, Vol 3 No 7, Jul 1986, pp 329-332.
3. M.S. Stix, et al., *IEEE J. QUANT. ELECTRON.*, Vol QE-19 No 4, Apr 1983, pp 520-525.
4. W. Seka, et al., *J. APPL. PHYS.*, Vol 49 No 4, Apr 1978, pp 2277-2280.
5. K.H. Drexhage, et al., *IEEE J. QUANT. ELECTRON.*, Vol QE-8 No 9, Sep 1972, p 759.
6. Yao Guangtao, et al., *ZHONGGUO JIGUANG [CHINESE JOURNAL OF LASERS]*, Vol 11 No 7, Jul 1984, pp 441-443.
7. Zhang Guifen [1728 6311 5358], et al., *GUANGXUE XUEBAO [ACTA OPTICA SINICA]*, Vol 2 No 6, Nov 1982, pp 496-499.
8. Wang Shijie [3769 0013 2638], et al., *ZHONGGUO JIGUANG*, Vol 16 No 8, Aug 1989, pp 489-492.
9. J. Emrry, et al., *J. APPL. PHYS.*, Vol 51 No 7, Jul 1980, pp 3548-3555.
10. Mang Yanping [5462 3601 5493], et al., *ZHONGGUO JIGUANG*, Vol 10 No 4, Apr 1983, pp 242-245.

Absolute Measurement of Laser Energy for 'Shen Guang' High-Power Laser Facility

91FE0626B Shanghai *GUANGXUE XUEBAO [ACTA OPTICA SINICA]* in Chinese Vol 11 No 5, May 91
pp 444-447 [MS received 2 Jul 90, revised 12 Nov 90]

[Article by Lin Kangchun [2651 1660 2504], Shen Liqing [3088 7787 7230], Tian Li [3944 5461], and Zhou Fuzheng [0719 1381 2973] of SIOFM, CAS: "Absolute Measurement of Laser Energy for 'Shen Guang' High-Power Laser Facility"]

[Text] Abstract: The characteristics of the absorption calorimeter used to measure laser energy output from the "Shen Guang" laser are described and its operating parameters are reported. It was used to measure the final-stage energy output of "Shen Guang," as well as the energies emitted at the front and middle stages and the energy associated with amplified spontaneous emission (ASE).

I. New Calorimeter for Laser Energy Measurement

The measurements of laser energy from Shen Guang¹ mainly include final-stage laser output, laser energy outputs from fixed points in the front and middle stages, and energy associated with ASE. Due to low sensitivity, poor surface response uniformity, and low resistance to

laser damage, a carbon calorimeter which had been used since 1960 could no longer satisfy the requirements for measuring energy output of the high-power laser. Therefore, a new absorption calorimeter was developed based on the development trend²⁻⁴ reported in other countries. Its principle and structure have been described elsewhere.⁵⁻⁶ Compared to a carbon calorimeter, this new absorption calorimeter has the following advantages.

1. Bulk Absorption

Laser energy is absorbed by the bulk, instead of the surface. The entire receiver absorbs the laser energy to avoid surface damage. A carbon calorimeter relies on surface absorption which is susceptible to damage by high-power lasers because the instantaneous temperature jump of the absorption layer, ΔT , is dependent upon the absorption coefficient A , energy density per unit area E , and laser pulsewidth Δt , i.e., ΔT is proportional to $AE\Delta t^{1/2}$. This is why a surface absorption calorimeter is easily damaged by an intense laser beam.⁷⁻⁸

2. Reliability and Accuracy

As we know, the receiving surface of a carbon funnel calorimeter is the inner surface of a cone and the laser is reflected several times to reach the top. There is a possibility of forming laser-induced plasma (gas) at the vertex when a high-power laser is concentrated there. Laser-induced plasma has a powerful effect in reflecting light. It may reflect the laser that arrives after the plasma is formed, which makes the measurement inaccurate. The new calorimeter employs an optically polished glass

receiver to prevent the formation of plasma. Its reflectance with respect to the laser can be measured. Therefore, the laser energy measurement is accurate and reliable.

3. High Sensitivity and Stability

The receiver of the new calorimeter uses several pairs of semiconductor P-N elements as thermoelectric transducers. Compared to the metallic wire elements used in a carbon calorimeter, its sensitivity is 1-2 orders of magnitude higher. Furthermore, P-N elements are rigidly soldered solids and their sensitivities remain unchanged after calibration. Hence, the receiver is very stable. A carbon calorimeter uses fine metallic wires as thermoelectric transducers. Its shape changes easily and cannot be fastened securely. Consequently, its sensitivity varies and performance becomes unstable.

4. Rapid Response and Recovery

This new calorimeter is three to five times faster in response, and 1-2 orders of magnitude shorter in measurement cycle compared to a carbon funnel calorimeter. This facilitates the experimental work, as well as the data analysis.

5. Absolute Measurement of Laser Energy

The absolute sensitivity of the new calorimeter can be calibrated by using the absolute energy of an electrical pulse to simulate the effect of the laser to be measured. This makes the laser energy measurement absolute.

The primary specifications of the new calorimeter are listed in Table 1. The 10-mm diameter aperture calorimeter (one unit) is used to measure ASE. The 20-mm and 25-mm diameter aperture calorimeters (four units each) are used to measure energy outputs from the front and middle stages. Two 80-mm diameter aperture

Table 1. Properties of Calorimeter

Aperture (mm)	φ 10	φ 20	φ 25	φ 80
Sensitivity (μV/J)	56,000	13,000	10,000	4,000
Wavelength (μm)	0.3-11	0.3-11	0.3-11	0.3-11
Response time (s)	1.5	2.0	2.5	4.0
Cooling const. (s ⁻¹)	0.033	0.018	0.012	0.005
Inhomogeneity	<+/-1%	<+/-1%	<+/-1%	<+/-2%
Repeat error	<+/-1%	<+/-1%	<+/-1%	<+/-1%
Inaccuracy	<+/-5%	<+/-5%	<+/-5%	<+/-5%

calorimeters are used for final stage laser energy output measurements.

The calibration of the new calorimeter is traceable to the national standards set by the China Institute of Metrology. The sensitivity of the new calorimeter is better than that of comparable devices^{4,9,10} developed by the Lawrence Livermore National Laboratory (LLNL) and Apollo Lasers Inc.

II. Measurement of Final-Stage Laser Energy Output

The "Shen Guang" has three final-stage energy output levels: 100 J/beam for 0.1 ns, 800 J/beam for 1 ns, and 960 J/beam for 3 ns. The maximum output power is 10^{12} W. To measure this kind of high-power laser, a colored neutral glass (AB₉) of some thickness is required as the absorber for the calorimeter. Its resistance to laser damage is 1-2 orders of magnitude higher than that of a carbon calorimeter. The final-stage energy output of the

"Shen Guang" measured 803 J (goal is 800 J) using a split-beam method in the national appraisal process. A calculation shows that this corresponds to a power load density of $1.2 \times 10^9 \text{ W/cm}^2$. The receiver of the calorimeter was inspected and found to be intact. After one year of use, the calorimeter was sent to the China Institute of Metrology for inspection. Its performance was found to

be consistent with the original calibration. This indicates that it is safe and reliable to use an 80-mm diameter aperture calorimeter for the measurement of final stage laser energy output from "Shen Guang." Table 2 shows some results of final-stage energy outputs of the south and north beams during target-irradiation experiments.

Table 2. Measured Energies of South and North Beam in Independent Run

No.	1	2	3	4	5	6	7	8	9	10
South beam (J)	351	400	434	405	475	502	511	503	490	539
North beam (J)	137	330	304	473	553	520	500	490	530	450

III. Measurement of Front and Middle Stage Fixed-Point Laser Energy

The purpose of setting a few points to measure laser energy at the front and middle stage includes (1) to check the stability of energy outputs at the front and middle stage to determine the source of instability in order to eliminate it in time during laser-fusion experiments, (2) to consciously adjust the amplifier voltage for optical pumping to control the final-stage energy output in order to satisfy various experimental requirements, and (3) to

adjust the front and middle stage amplifier voltage levels of the south and north beam to achieve an ideal balance and uniform illumination compression when both beams are synchronized for the same target. Table 3 shows that the maximum deviation in energy between the south and north beam is approximately 15 percent. Nevertheless, if we can carefully adjust the ratio of the light source voltages at the front and middle stages, the energy imbalance can be reduced to 10 percent or less to obtain very satisfactory experimental data.

Table 3. Unbalances of Beam Energies in Counter Direction With Synchronization

No.	1	2	3	4	5	6	7	8	9	10
South beam (J)	25.9	55.0	151.7	99.9	61.7	37.4	49.7	58.8	58.5	73.2
North beam (J)	21.2	52.0	159.1	113.9	63.2	33.9	54.2	63.2	64.0	76.0
Unbalance (%)	13	1	11	20	9	4	15	13	15	10

IV. ASE Measurement

The amplified spontaneous emission (ASE) of a laser system is the energy emitted without the oscillator while other amplifiers are turned on for a normal run. The ASE output pulse is of the same order as the optical pump pulsewidth. The front portion is the "leading laser" that reaches the target surface. This ASE "leading laser" is focused on the target by a lens. Although it is very small, it is nonetheless deleterious to the fusion experiment if it exceeds a certain value. During the appraisal of "Shen Guang", ASE energy was found to be within 0.7-0.8 mJ in either the north or south beam. It is much lower than the original target of 2 mJ. However, it still burned through an 0.2- μm thick aluminum foil placed at the target point. Even at 0.4 mJ, it is capable of leaving a burn mark on an aluminum target and additional isolation is required. Only when ASE is reduced to below 0.1 mJ can a 80- μm diameter hollow glass target with an 0.5- μm thick wall be free from destruction. This indicates that ASE must be reduced to this level to satisfy the requirements for laser-induced fusion experiments. The measurement of such minute energy at 0.1 mJ level can only be done accurately with a high-sensitivity, high-resolution calorimeter with a 10-mm diameter aperture.

The authors wish to express their gratitude to Ge Luyan [5514 7216 5333], Zhang Honglin [1728 3163 2651], Liu

Fengchi [0491 7364 5041], Huang Guanlong [7806 7070 7893], Dai Dazhi [2071 6671 2535], Wu Fengchun [0702 6646 2504], and Cai Xijie [5591 1585 3381] for their assistance and to Lin Zunqi [2651 1415 3825] for reviewing this manuscript.

References

1. Yu Wenyan [0151 2429 3508] and Lei Shizhan [7191 0099 3277], ZIRAN ZAZHI [NATURE], Vol 11 No 5, May 1988, p 352.
2. R.L. Smith, et al., IEEEET, Vol IM-21 No 2, Nov 1972, p 434.
3. G.E. Chamberlain, et al., Ibid., Vol IM-27 No 1, Mar 1978, p 81.
4. S.R. Gunn, LLNL report UCID-17308, 1976.
5. Lin Kangchun, Zhou Fuzheng, et al., ZHONGGUO JIGUANG [CHINESE JOURNAL OF LASERS], Vol 10 No 3, Mar 1983, p 186.
6. Ibid., HE JUBIAN YU DENGLIZITI WULI [NUCLEAR FUSION AND PLASMA PHYSICS], Vol 3 No 1, Mar 1983, p 41.

7. S.R. Gunn, REV. SCI. INSTRUM., Vol 45 No 7, Jul 1974, p 936.
8. D.L. Franzen and L.B. Schmidt, APPL. OPT., Vol 15 No 12, Dec 1976, p 3115.
9. Xiang Liren [0686 4539 0086], JIGUANG [LASERS], Vol 6 No 9, Sep 1979, p 58.
10. ALC Laser Corp. [U.S. firm] 1984 product brochure.

Inhomogeneous Distribution of Electron Density, Strong X-Ray Emission by Laser Irradiated Segmented Planar Target

91P60207 Shanghai ZHONGGUO JIGUANG [CHINESE JOURNAL OF LASERS] in Chinese Vol 18 No 5, May 91 pp 321-323 [MS received 18 May 89]

[Article by Feng Xianping [7458 6343 1627], Xu Zhizhan [1776 5267 1455], et al., of the CAS Shanghai Institute of Optics and Fine Mechanics (SIOFM), 201800: "Extremely Inhomogeneous Distribution of Interface Electron Density Induced by Laser Irradiation of Dual-Segment Targets, Strong X-Ray Emission"]

[Summary] In research on laser ICF and on X-ray lasers where plasma is the active medium, the plasma must have a relatively high homogeneity to satisfy requirements for inward compression and X-ray amplification. In actual practice, however, several mechanisms have been known to cause inhomogeneities at the target surface,^{1,2} so a study of these mechanisms is critical to further progress in the fields. In the current study, research on the plasma dynamics and radiation characteristics at the interface (seam) between the two segments of an Al-Al segmented target is reported. Experimental equipment includes SIOFM's six-path high-power Nd-glass laser facility, a visible-light probe, and an X-ray pinhole camera. A schematic of the experimental setup is shown in Figure 1.

After joining two of the laser beam paths together, the laser output wavelength was 1.06 μm , pulsewidth was 250 ps, and energy was variable from 4 to 25 Joules. Focused via an aspherical lens/cylindrical lens assembly, the laser beam at the target surface was 1.6 mm long and 0.1 mm wide (half-power point); on-target power density ranged from $(1-6) \times 10^{13} \text{W/cm}^2$. Figure 2 [photograph not reproduced] depicts the laser-plasma X-ray optical field intensity distribution at the Al-Al interface with a power density of $5 \times 10^{13} \text{W/cm}^2$, while Figure 3 [photograph not reproduced] shows a shadowgram, taken 1.7 ns after the laser peak, of the plasma with the probing beam orthogonal to the 1.6-mm long focal line. Figure 4 [photograph not reproduced] shows an interferogram of the plasma, and Figure 5 [photograph not reproduced] shows the corresponding shadowgram when laser power density was reduced to $2 \times 10^{13} \text{W/cm}^2$.

Results can be summarized as follows: 1) the plasma at the segmented Al-Al target seam region has a very high

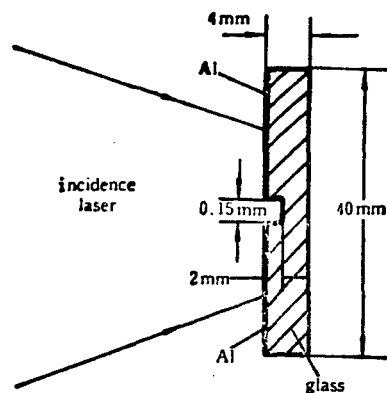


Figure 1. Schematic of the Experimental Setup for Line-Focused Laser Irradiation Segmented Planar Target

electron density with an extremely inhomogeneous distribution, and 2) X-rays emitted in this region are much more intense than those emitted in regions without a seam.

References

1. P. Jaegle, et al., J. OPT. SOC. AM., B, Vol 4 No 4, 1987, pp 563-574.
2. M.G. Haines, et al., PHYS. REV. LETT., Vol 47 No 3, 1981, pp 917-920.
3. Z.Z. Xhu, et al., PHYS. REV., A, Vol 39 No 2, 1989, pp 808-813.
4. Feng Xianping, et al., LIANGZI DIANZIXUE [QUANTUM ELECTRONICS], Vol 5 No 4, 1988, pp 332-336.
5. Jiang Zhiming, et al., ZHONGGUO KEXUE [SCIENTIA SINICA], Series A, No 4, 1989, pp 313-318.

Automatic Tuning Picosecond Parametric Laser

91FE0722A Shanghai GUANGXUE XUEBAO [ACTA OPTICA SINICA] in Chinese Vol 11 No 6, Jun 91 pp 525-530 [MS received 20 Jul 90, revised 16 Nov 90]

[Article by He Huijuan [0149 1979 1227], Lu Yutian [7120 7183 3944], Dong Jingyuan [5516 2529 0337], Zhao Qingchun [6392 1987 2504], and Li Yongchun [2621 3057 2504] of the Laser Technology Development Laboratory of CAS SIOFM: "Automatic Tuning Picosecond Parametric Laser"]

[Text] Abstract: A pair of MgO:LiNbO_3 crystals are used for angle tuning to produce an output tunable in the infrared band of 0.7-2.2 μm . The apparatus is also equipped with an automatic wavelength scanning system. Factors affecting the pulsewidth and linewidth are analyzed. The analysis agrees with the experimental results. The pulsewidth is less than 30 ps and the linewidth is approximately 1 nm (10 nm in the vicinity of degenerate wavelength). A single pulse has peak power

of the order of MW. The overall energy conversion efficiency of the parametric laser is 5.4 percent.

I. Introduction

Due to low conversion efficiency of infrared dyes and narrow tunable range using other means such as color-center crystals and Raman technique, parametric conversion has become the major method to produce a wide-tunable-band ultra-short infrared laser pulse. The tunable range of a parametric oscillator is limited by the cavity resonator membrane. It is difficult to make a wideband membrane highly resistant to damage. The crystal in the cavity is easily damaged. Furthermore, there is the disadvantage of output pulse widening by group velocity dispersion. Although the gain of a traveling-wave parametric system is low, it is capable of avoiding these problems. The parametric light pulse is further compressed by the pumping light pulse. The spectral purity and directivity are also better. Moreover, the parametric pulse and pumping pulse are precisely synchronized. This is good for direct frequency mixing and synchronous measurement.

In recent years, further study has been done on picosecond infrared parametric lasers. In 1980, Seilmeier¹ used the second harmonic (529 nm) of an Nd:glass laser to pump a pair of LiNbO₃ crystals; in addition, low-temperature tuning was used to fill the wavelength void to obtain ps light output over 0.6-3.7 μm . In 1983, Wordzsek² used the third harmonic (353 nm) of an Nd:glass laser to pump an ADP crystal to obtain ps light output from 0.4-1.1 μm . In 1987, Anthon³ used the third harmonic (355 nm) of an Nd:YAG laser to pump a KDP crystal to obtain ps light output in the 0.45-0.65 μm and 0.8-1.6 μm ranges; these were achieved by using a traveling-wave parametric system. Jonushauskas⁴ employed the second harmonic wave (535 nm) of a lanthanum beryllium oxide laser to pump a parametric oscillator with three different crystals and made a comparison.

In this work, the second harmonic wave (535 nm) of a Nd:YAG laser is used to pump a pair of MgO:LiNbO₃ crystals and results in ps laser pulses covering the 0.7-2.2 μm band.

II. Experimental Scheme

A pair of nonlinear crystals are used to form a traveling-wave parametric system. A part of the pumping light is converted by the first crystal to fluorescence, conjugate to the wavelength of the signal and idle light. The fluorescence is generated in the spontaneous parametric system. Because of off-axis phase mismatch, it has a considerable spectral-linewidth and a large divergence angle. This fluorescence and the remaining pumping light are parametrically amplified in the second crystal. It only amplifies the spectral component corresponding to the narrow-linewidth pumping light. Hence, it results in a narrow parametric light output.

Energy and momentum conservation should be obeyed among signal light (expressed by subscript s), idle light (subscript i), and pumping light (subscript p), i.e.

$$\frac{1}{\lambda_p} = \frac{1}{\lambda_s} + \frac{1}{\lambda_i}, \quad (1)$$

$$\frac{n_p}{\lambda_p} = \frac{n_s}{\lambda_s} + \frac{n_i}{\lambda_i}, \quad (2)$$

where n is the index of refraction of the crystal. By properly choosing the pumping wavelength and nonlinear crystal and its orientation, it is possible to satisfy the phase-matching conditions (1) and (2) to produce a parametric light at the desired wavelength.

Complete range of angular tuning to fill the vicinity of the degenerate point^{1,5} is only possible at low-temperature when using the second harmonic (532 nm) of a Nd:YAG laser to pump conventional LiNbO₃ crystals. Magnesium-doped LiNbO₃ not only has a complete angular tuning range at high temperature but also has a higher threshold of resistance against damage.⁶ In this work MgO:LiNbO₃ (prepared by Shanghai Institute of Silicates, CAS) was used as the nonlinear crystal.

The crystal was cut in the Z-73° direction. It was maintained at a constant temperature of 72.8°C. It was operated according to type-I phase-matching condition (e to o + o). When the internal angle θ varies between $\pm 12^\circ$, the crystal's tuning range covers 0.7-2.2 μm . The tuning curve is shown in Figure 1. There is an excellent agreement between experimental data and theoretical computation. The crystal is 6 x 12 x 26 mm in size. A 5-mm diameter pumping beam passes through it. This aperture is ensured over the range of tuning angle. The length is there to ensure a sufficient gain.

Wavelength tuning is done by using a single-board-controlled stepper motor to adjust the crystal

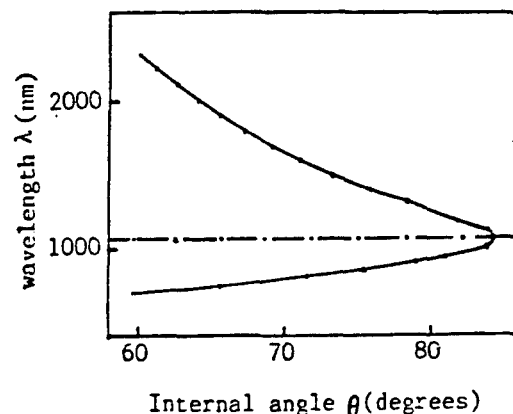


Figure 1. Angular Tuning Curve; Line: Theory, Dots: Experimental Points

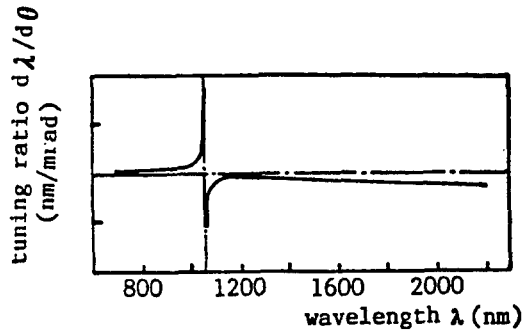


Figure 2. Angular Tuning Ratio Curve

platform. The two crystals are synchronized to rotate at an accuracy of 0.01°. It is also accompanied with a lateral movement to ensure the aperture of light passage. An angular tuning curve may be derived from the tuning curve, as shown in Figure 2. Obviously, except very close to the degenerate point, the wavelength error is less than 1 nm when the crystal angle is adjusted in steps of 0.01°. This means that the tuning accuracy is always better than the spectral-linewidth of the parametric light; it is also better than the wavelength resolution (1 nm).

The index of refraction of LiNbO₃ depends heavily on temperature. Temperature variation can seriously affect the stability of the parametric light. Figure 3 shows a temperature sensitivity curve as a function of wavelength. It is derived by differentiating the angular tuning curve with respect to temperature. When the crystals are maintained within $\pm 0.1^\circ\text{C}$, the stability of the wavelength of the parametric light is of the same order as the tuning accuracy. It is better than the spectral-linewidth and wavelength resolution (other than in the vicinity of the degenerate point).

The linewidth and divergence angle of the pumping light have an influence on the linewidth of the parametric light. The pulsewidth of the pumping light is also directly proportional to the pulsewidth of the parametric light. Therefore, in order to obtain a high-quality parametric beam, it is imperative to have a pumping source with a sharp pulse, narrow linewidth, and small divergence

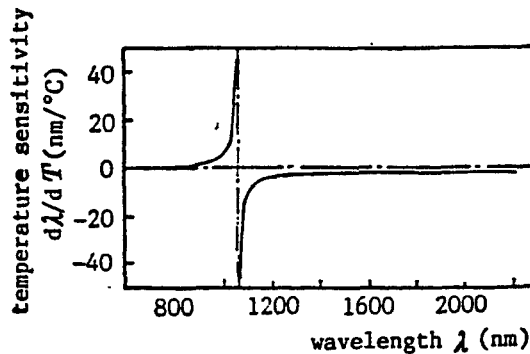


Figure 3. Temperature Sensitivity Curve

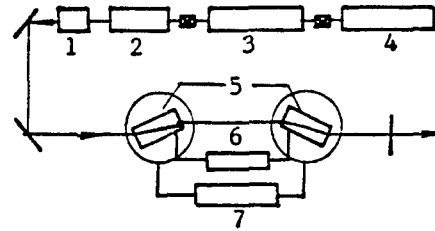


Figure 4. Schematic of the Automatic Tunable Picosecond Parametric Laser

Key: 1. SHG; 2. Amplifier; 3. Single pulse selector; 4. ps YAG laser; 5. MgO:LiNbO₃; 6. Thermostat; 7. Tuning control

angle. The pumping source is a ps Nd:YAG laser system with a very high pulse repetition frequency (prf). It consists of an oscillator, amplifier, single-pulse selector, and frequency doubler. The oscillator is a high-prf active-passive mode-locked YAG laser⁷ with a thermally stable cavity. The signal-pulse selector uses an avalanche-photodiode-controlled Pockels switch to pick a pulse⁸ from a train of pulses. The beam is expanded, amplified, and frequency-doubled to become a single laser pulse at 532 nm. Its pulsewidth is 30-50 ps, linewidth is 0.05 nm, and divergence angle is 0.2 mrad.

Figure 4 shows the schematic diagram of the experiment.

The divergence angle of the parametric light is significantly affected by the space between the two crystals. Figure 5 shows the experimental data. When the gap increased from 5 cm to 50 cm, the angle decreases sharply from 200 mrad to below 10 mrad. However, the improvement becomes more gradual by widening the gap farther and the energy output drops off more. As a compromise, the space between the two crystals was set at 60 cm. At 700 nm, the typical divergence angle is < 3 mrad.

III. Characteristics of Parametric Light

The parametric gain, G , is a function of the pulsewidth of the parametric light, τ_s , and that of the pumping light, τ_p :

$$\frac{\tau_s}{\tau_p} = \left(\frac{1}{2} \ln G \right)^{-1/2} \quad (3)$$

The traveling-wave parametric amplifier is treated by a planar wave model and its gain G is^{9,10}:

$$G = \cosh^2 \Gamma l \quad (4)$$

$$\Gamma = \left(\frac{\mu_0}{\epsilon_0} \right)^{3/4} d_{eff} \left(\frac{2\omega_s \omega_i I_p}{n_s n_i n_p} \right)^{1/2}$$

where l is the effective length of parametric amplification, Γ is the gain factor, μ_0 is the magnetic permeability in vacuum, ϵ_0 is the dielectric constant in vacuum, d_{eff} is

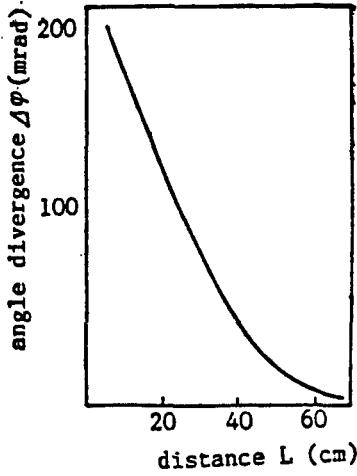


Figure 5. Angle Divergence of the Parametric Beam Versus Distance Between the Two Crystals

the effective nonlinear coefficient, I_p is the pumping power density, ω is the light frequency, and n is the index of refraction.

Actually, the laser has $I_p = 1 \times 10^8 \text{ W/cm}^2$, $l = 2.6 \text{ cm}$, $d_{\text{eff}} = d_{31} \sin(73^\circ \pm 12^\circ)$ equals approximately $3 \times 10^{-23} \text{ c/v}^2$, and $\omega_s \omega_i = (2.3-3.2) \times 10^{30}$. From equations (3) and (4), (τ_s/τ_p) equals approximately $(1/1.6)$. The pulsewidth was measured to be $< 30 \text{ ps}$ (FWHM) with a streak camera over the entire tuning range and $(\tau_s/\tau_p) = 1/(1.4-1.7)$. This indicates that the experimental data agrees well with theoretical calculation.

The spectral-linewidth of the parametric light, $\Delta\lambda$ comes from four areas¹:

1. Linewidth due to phase mismatch ΔK :

$$\left. \begin{aligned} \Delta\lambda_1 &= 2 \left| \frac{d\lambda}{dK} \right| |\Delta K|, \\ \frac{d\lambda}{dK} &= \frac{\lambda^2}{2\pi(n_{\text{eff},s} - n_{\text{eff},i})}, \quad n_{\text{eff}} = n + \lambda \frac{dn'}{d\lambda} \end{aligned} \right\} (5)$$

where $(dn/d\lambda)$ is the optical dispersion of the nonlinear crystal. When a small signal is amplified exponentially, with phase mismatch ΔK the gain factor is^{10,11}:

$$\Gamma = \left(\Gamma^2 - \frac{\Delta K^2}{4} \right)^{1/2}, \quad (6)$$

Let us allow the gain to drop by one-half as the tolerable mismatch ΔK , i.e., $\exp(2\Gamma l) = (1/2)\exp(2\Gamma_1 l)$, then:

$$\Delta K = 2\sqrt{\ln 2} \sqrt{\Gamma/l} \quad (7)$$

2. Linewidth contributed by angular divergence of the pumping light ϕ :

$$\Delta\lambda_2 = \frac{d\lambda}{d\theta} \cdot \frac{\phi}{n_p}, \quad (8)$$

where $(d\lambda/d\theta)$ is the angular tuning rate which can be directly derived by differentiating the tuning curve, or by using the following equation:

$$\frac{d\lambda}{d\theta} = \frac{n_p^2 \lambda_s^2}{2(n_{\text{eff},s} - n_{\text{eff},i}) \lambda_p} \cdot \frac{(n_p^o)^2 - (n_p^o)^2}{(n_p^o)^2 \cdot (n_p^o)^2} \sin 2\theta. \quad (9)$$

3. Linewidth due to the discrete angle α between the parametric light and the pumping light:

$$\left. \begin{aligned} \Delta\lambda_3 &= \alpha^2 \frac{n_p \lambda_s \lambda_i}{2(n_{\text{eff},s} - n_{\text{eff},i}) n_i n_s \lambda_p}, \\ \alpha &= \frac{d}{L}, \end{aligned} \right\} (10)$$

where d is the diameter of the pumping beam and L is the distance between the two crystals.

4. Linewidth due to the width of the pumping light $\Delta\lambda_p$:

$$\Delta\lambda_4 = 0.3 \frac{n_{\text{eff},p} - n_{\text{eff},i}}{n_{\text{eff},s} - n_{\text{eff},i}} \frac{\lambda_s^2}{\lambda_p^2} \Delta\lambda_{p0} \quad (11)$$

The above shows that linewidth varies with wavelength. It is narrower on the shorter-wavelength end and wider on the longer-wavelength end. It is considerably wider at the degenerate wavelength $1.064 \mu\text{m}$. Measurements were made with a CCD array after the light passed through a monochromator. Its output signal was collected and stored by a microcomputer. The spectral frequency curve is displayed on an oscilloscope or printed out. Figure 6 shows some typical spectral profiles. Table 1 shows a comparison of the calculated values and experimental results, which are in very good agreement.

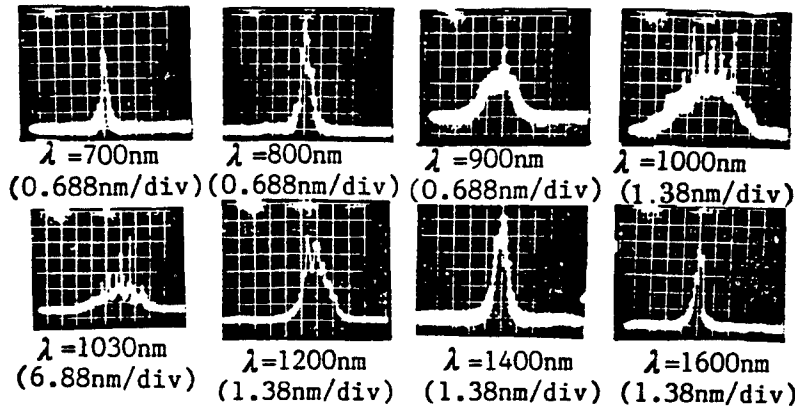


Figure 6. Spectral Profiles of the Parametric Pulses, Obtained From CCD Spectrograph

Table 1. Spectral Bandwidths of the Parametric Pulses; Calculated Values and Experimental Results Are Compared (nm)

λ	700	800	900	1000	1030	1200	1400	1600	1800	2000	2200
$\Delta\lambda_1$	0.13	0.26	0.58	2.0	4.6	1.9	1.1	1.1	1.2	1.3	1.4
$\Delta\lambda_2$	0.04	0.06	0.08	0.18	0.34	0.18	0.19	0.23	0.29	0.35	0.42
$\Delta\lambda_3$	0.3	0.4	0.7	1.8	3.8	1.0	0.5	0.4	0.4	0.3	0.3
$\Delta\lambda_4$	0.03	0.06	0.14	0.44	1.0	0.28	0.15	0.12	0.11	0.1	0.07
$\Delta\lambda$ calculated	0.3	0.5	1.0	2.7	6.1	1.9	1.1	1.1	1.2	1.3	1.4
$\Delta\lambda$ measured	0.3	0.5	1.3	4.0	8.0	1.9	1.2	1.2		1.4	

IV. Conclusions

A picosecond traveling-wave parametric laser system was developed based on angular tuning of a pair of MgO:LiNbO₃ crystals. It operates in a wide range between 0.7 and 2.2 μm . A high quality, high-power single-pulse output of the order of picoseconds is obtained. The pulsewidth is <30 ps, linewidth is 1 nm (approximately 10 nm at the degenerate point), and single-pulse peak power is at the MW level. The overall parametric energy-conversion efficiency is 5.4 percent. In addition, the apparatus is equipped with an automatic wavelength tuning and display system.

Qian Linxing [6929 2651 5281], Gu Shengru [7357 5110 1172], Zhao Longxing [6392 7127 5281], and Guo Jinghua [6753 2533 5478] also participated in this work. The authors wish to thank Qiao Futang [0829 4395 1016] of the CAS SIOFM for providing high-precision mechanical design and to Li Qingguo [2621 1987 0948] for supplying high-quality cutoff filters.

References

1. A. Seilmeier and V. Kaiser, APPL. PHYS., Vol 23 No 2, Feb 1980, pp 113-119.
2. F. Wordrazek, et al., Ibid., Vol B32 No 1, Jan 1983, pp 39-42.
3. D.W. Anthon, et al., REV. SCIENT. INSTRUM., Vol 58 No 11, Nov 1987, pp 2054-2059.

4. G. Jonushauskas, et al., SOVIET J. QUAN. ELECTRON., Vol QE-17 No 10, Oct 1987, p 1303-1304.
5. Honer Fay, et al., APPL. PHYS. LETT., Vol 12 No 3, 1 Feb 1968, pp 89-92.
6. P.M. Bridenbaugh, et al., Ibid., Vol 17 No 3, 1 Aug 1970, pp 104-106.
7. He Huijuan, et al., ZHONGGUO JIGUANG [CHINESE JOURNAL OF LASERS], Vol 10 No 11, Nov 1983, pp 765-769.
8. Li Yongchun, et al., Ibid., Vol 11 No 3, Mar 1984, pp 170-172.
9. G.A. Massey, et al., IEEE QUANT. ELECTRON., Vol QE-12 No 2, Feb 1976, pp 143-147.
10. S.E. Harris, PROC. IEEE, Vol 57 No 12, Dec 1969, pp 2096-2113.
11. A. Seilmeier, et al., OPT. COMMUN., Vol 24 No 3, Mar 1978, pp 237-242.

Additional Details on Domestically Developed 10 kW CO₂ Laser Revealed

91P60259A Shanghai ZHONGGUO JIGUANG [CHINESE JOURNAL OF LASERS] in Chinese Vol 18 No 6, Jun 91 p 457

[Article by Ji Zhong [4764 6988]: "China Develops New 10,000-Watt CO₂ Laser"; cf. earlier report in JPRS-CST-91-010, 17 May 91 p 35]

[Summary] The CAS Shanghai Institute of Optics & Fine Mechanics [SIOFM] has developed a new 10 kW transverse-flow CO₂ laser with dimensions of 2 m x 2 m x 2.5 m. The expert appraisal group has certified that this state-of-the-art CO₂ laser has the following specifications: multimode running-time output power is over 10 kW, with an electrooptical conversion efficiency of 14 percent; low-order-mode running-time output power is 6 kW, with an electrooptical conversion efficiency of 8.3 percent; beam divergence angle (full angle) is 2.2 milliradians; and single-gas-filling CW operation is 8 hours at a 10 kW-plus power level.

Broadband Frequency-Doubled Nd:Glass Laser Built at SIOFM

91P60269A Beijing ZHONGGUO KEXUE BAO
[CHINESE SCIENCE NEWS] in Chinese 5 Jul 91 p 2

[Article by Shang Guang [1424 0342]: "Broadband Frequency-Doubled Neodymium:Glass Laser Apparatus Completed"]

[Summary] Shanghai (ZHONGGUO KEXUE BAO wire report)—The broadband frequency-doubled Nd:glass laser apparatus developed in a 10-year effort by researchers from the CAS Shanghai of Optics & Fine Mechanics (SIOFM) passed CAS-level technical appraisal on 10 June. This high-power apparatus, used in laser fusion research to implement high-density target compression via laser direct drive has been developed only by a small number of other nations, including the United States and Japan.

The development of this new laser apparatus indicates that SIOFM has overcome problems such as broadband three-wave nonlinear wave coupling in a Q-switched laser, suppression of nonlinear effects, and the requirement for directionality of the frequency-doubled laser beam to be superior to the directionality of the fundamental-frequency beam. The completion of this apparatus represents a major improvement to SIOFM's LF12 laser fusion facility, and will provide a valuable research tool in developing even larger-scale laser fusion equipment.

Soft X-Ray Picosecond Framing Camera Developed

91P60269F Beijing ZHONGGUO KEXUE BAO
[CHINESE SCIENCE NEWS] in Chinese 19 Jul 91 p 1

[Article by Wang Baizhan [3769 4102 2069]: "Soft X-Ray Picosecond Framing Camera Unveiled"]

[Summary] Xian (ZHONGGUO KEXUE BAO wire report)—A soft X-ray picosecond (ps) framing camera recently developed by the [CAS] Xian Institute of Optics & Fine Mechanics (XIOFM) has passed CAS-level appraisal. The experts have certified that this state-of-the-art apparatus will provide a powerful diagnostic tool for domestic research in inertial confinement fusion and X-ray lasers. Only France, the United States, Great Britain, Japan, the Soviet Union, and now China have developed this advanced equipment. The XIOFM-developed apparatus has a 250-ps exposure time and a dynamic spatial resolution of five lines per millimeter.

5285 FORT ROYAL RD
SPRINGFIELD VA

2216

This is a U.S. Government publication. Its contents in no way represent the policies, views, or attitudes of the U.S. Government. Users of this publication may cite FBIS or JPRS provided they do so in a manner clearly identifying them as the secondary source.

Foreign Broadcast Information Service (FBIS) and Joint Publications Research Service (JPRS) publications contain political, military, economic, environmental, and sociological news, commentary, and other information, as well as scientific and technical data and reports. All information has been obtained from foreign radio and television broadcasts, news agency transmissions, newspapers, books, and periodicals. Items generally are processed from the first or best available sources. It should not be inferred that they have been disseminated only in the medium, in the language, or to the area indicated. Items from foreign language sources are translated; those from English-language sources are transcribed. Except for excluding certain diacritics, FBIS renders personal and place-names in accordance with the romanization systems approved for U.S. Government publications by the U.S. Board of Geographic Names.

Headlines, editorial reports, and material enclosed in brackets [] are supplied by FBIS/JPRS. Processing indicators such as [Text] or [Excerpts] in the first line of each item indicate how the information was processed from the original. Unfamiliar names rendered phonetically are enclosed in parentheses. Words or names preceded by a question mark and enclosed in parentheses were not clear from the original source but have been supplied as appropriate to the context. Other unattributed parenthetical notes within the body of an item originate with the source. Times within items are as given by the source. Passages in boldface or italics are as published.

SUBSCRIPTION/PROCUREMENT INFORMATION

The FBIS DAILY REPORT contains current news and information and is published Monday through Friday in eight volumes: China, East Europe, Soviet Union, East Asia, Near East & South Asia, Sub-Saharan Africa, Latin America, and West Europe. Supplements to the DAILY REPORTs may also be available periodically and will be distributed to regular DAILY REPORT subscribers. JPRS publications, which include approximately 50 regional, worldwide, and topical reports, generally contain less time-sensitive information and are published periodically.

Current DAILY REPORTs and JPRS publications are listed in *Government Reports Announcements* issued semimonthly by the National Technical Information Service (NTIS), 5285 Port Royal Road, Springfield, Virginia 22161 and the *Monthly Catalog of U.S. Government Publications* issued by the Superintendent of Documents, U.S. Government Printing Office, Washington, D.C. 20402.

The public may subscribe to either hardcover or microfiche versions of the DAILY REPORTs and JPRS publications through NTIS at the above address or by calling (703) 487-4630. Subscription rates will be

provided by NTIS upon request. Subscriptions are available outside the United States from NTIS or appointed foreign dealers. New subscribers should expect a 30-day delay in receipt of the first issue.

U.S. Government offices may obtain subscriptions to the DAILY REPORTs or JPRS publications (hardcover or microfiche) at no charge through their sponsoring organizations. For additional information or assistance, call FBIS, (202) 338-6735, or write to P.O. Box 2604, Washington, D.C. 20013. Department of Defense consumers are required to submit requests through appropriate command validation channels to DIA, RTS-2C, Washington, D.C. 20301. (Telephone: (202) 373-3771, Autovon: 243-3771.)

Back issues or single copies of the DAILY REPORTs and JPRS publications are not available. Both the DAILY REPORTs and the JPRS publications are on file for public reference at the Library of Congress and at many Federal Depository Libraries. Reference copies may also be seen at many public and university libraries throughout the United States.